Politecnico di Milano

Scuola di Ingegneria Industriale e dell'Informazione

Corso di Laurea Magistrale in Engeneering Physics

Sub-Doppler precision laser spectroscopy of trifloromethane at 8.6 μm

Supervisor: Dr. Gianluca GALZERANO

Co-supervisor: Dr. Alessio Gambetta

Master Thesis of:
Edoardo VICENTINI
Matr. 841450

Academic Year 2016-2017

Contents

List of Figures

List of Tables

Acknowledgements

I would like to express my deep gratitude toward Dr. Gianluca Galzerano, my thesis supervisor, for his patient guidance, warm encouragement and useful critiques of this thesis work. Special thanks go to my co-supervisor Dr. Alessio Gambetta for his help and guidance for the laboratory experiments. I would like also to thank Dr. Nicola Coluccelli, Dr. Toney Fernandez and Eng. Yuchen Wang for their support and advice each time I asked. Finally, I would like to thank my family for their backing and patience.
Superamici 4evah.

Abstract

This experimental thesis describes the spectroscopy in the sub-Doppler regime of trifluoromethane, CHF_3, in the medium infrared spectral region (vibrational band ν_5) by a single-mode quantum cascade laser at 8.6 μm. Measurements were perform using a middle-infrared optical frequency comb generated by a frequency difference process, which was frequency stabilized with respect to a Rb clock referenced to the GPS.

In particular, two different methodologies are presented. The first one consists on the quantum cascade laser frequency stabilization against a saturated absorption of the CHF_3 and on the absolute measure of the line center frequencies through the mid-infrared comb. The second involves the quantum cascade laser locking to an optical frequency comb tooth and spectroscopic registration of saturated absorption by tuning the comb repetition frequency. This first methodology showed relative precision at level of 10^{-12} (corresponding to 10^2 Hz) in determining the central absorption frequencies. By the second technique, the line broadening for pressure and the saturation intensities of CHF_3 to 8.6 μm were also measured.

Sommario

Questa tesi sperimentale descrive la spettroscopia in regime di saturazione (sub-Doppler) del trifluorometano, CHF_3, nella regione del medio infrarosso (banda vibrazionale ν_5) mediante laser a cascata quantica con emissione in singolo modo e una lunghezza d'onda di 8.6 μm. Le misure sono state effettuate utilizzando un pettine di frequenza ottico nel medio infrarosso generato per differenza di frequenza, stabilizzato in frequenza rispetto ad un orologio al Rb asservito al GPS.

In particolare sono presentate due differenti metodologie di misure. La prima consiste nello stabilimento in frequenza del laser a cascata quantica rispetto ad un assorbimento saturo del CHF_3 e le misura assoluta delle frequenze del centro riga mediante il pettine nel medio infrarosso. La seconda prevede invece l'aggancio in fase del laser a cascata quantica ad un dente del pettine di frequenza e la registrazione spettroscopica degli assorbimenti saturi mediante la sintonizzazione della frequenza di ripetizione del pettine. La prima metodologie ha dimostrato precisioni relative di 10^{-12} (corrispondenti a $3 \cdot 10^3$ Hz) nella determinazione delle frequenze centrali degli assorbimenti. Mediante la seconda tecnica, sono state misurate anche gli allargamenti di riga per pressione e potenza e le intensità di saturazione del CHF_3 a 8.6 μm.

Introduction

For more than half a century, laser spectroscopy has played a crucial role in probing molecular structure and dynamics. Over the past decade high- resolution and broadband spectroscopy has received a major boost from the advent of optical frequency combs, highly-coherent light sources constituted by an array of evenly spaced optical narrow lines whose absolute frequencies are known with a fractional accuracy of 10^{-16} or even better. Originally developed to provide a direct link between the optical and radio-frequency (RF) domains (2005 Nobel prize for Physics to T. W. Hänsch and J. L. Hall "for their contributions to the development of laser-based precision spectroscopy, including the optical frequency comb technique" [1][2]), optical frequency combs have spread in many other research areas such as attosecond science, optical waveform generation, remote sensing and distance measurements, low-phase- noise microwave synthesis, optical communications, and astrophysics. Among the wide spectrum of fields affected by the advent of frequency combs, broadband and precision spectroscopy plays a key role since it is an invaluable tool for a variety of applications in physics, chemistry, biology, medicine, and environmental sciences. The availability of a frequency comb, hundreds of thousands of precise and accurate optical lines in a single optical source, allows to a spectroscopic instrument the unique combination of large bandwidth and high spectral resolution. Two general approaches have emerged for frequency comb application as a spectroscopic tool. In the first approach, the optical frequency comb serves simply as a frequency ruler against which a continuous-wave (cw) probe tunable laser is referenced. Once locked to the n-th comb line, the absolute frequency of the cw laser can be scanned across a desired molecular absorption by fine tuning of the comb tooth spacing frequency (the so called comb repetition frequency). This approach is preferred when a single or few absorption line have to be measured with highest frequency precision and sensitivity. The second general approach employs the optical frequency comb to directly probe atomic and molecular samples and is called direct comb spectroscopy [3].

Thanks to the breakthrough technologies originating respectively from the world of ultracold quantum gases and that of femtosecond laser frequency combs during the last decades, methods of precision spectroscopy have advanced to the point where atomic/molecular transition frequencies can be determined with an astonishing precision (down to a few parts in 10^{18}), to such an extent that detecting the influence of fundamental new physics at the eV energy scale is now within reach [4]. In this frame, more and more challenging experiments are underway, aiming at testing nature symmetries and constants with unprecedented sensitivity. In particular, in the last few years a strong interest has focused on the possibility that what we know as the fundamental physical constants might show variations over cosmological time scales. Such an effect arises quite naturally in modern theories (Lie Groups, String/M Theories, . . .) attempting either to establish a Grand Unification Theory beyond the Standard Model or to reconcile this latter and General Relativity in a Theory of Everything[5][6][7]. Since variation of dimensional constants cannot be distinguished from that of the units, it makes

more sense to consider changes of dimensionless parameters. The prime target is the fine structure constant, $\alpha = e^2/4\pi\epsilon_0\hbar c$, which defines the scale of quantum electrodynamics; the second prominent quantity is the proton-to-electron mass ratio, $\beta = m_p/m_e$, which characterizes the strength of strong interaction in terms of the electro-weak one. While in the former case the temporal stability is conveniently probed through atomic transitions [8], the β ratio is more accurately addressed with molecular systems where resorting to the inaccurate nuclear Schmidt model is bypassed. One approach is to compare the frequencies of molecular lines measured in the present epoch on Earth with the corresponding ones from astronomical objects at high redshifts [9][10].

Concerning β ratio, a possible approach is a ultra-high resolution two-photon spectroscopy with a molecular beam with intense flux, low temperature, and reduced longitudinal speed. This will be attained by combining buffer-gas cooling and Stark manipulation. Since buffer-gas cooling operates with nearly all species, potentially any molecule with a relatively high electric dipole moment (EDM) and a favorable two-photon transition may be chosen for the experiment. The fluoroform (CHF_3) molecule exhibits both these features and it has been selected for measurement of β ratio and its temporal variance [11]. Beside that CHF_3, or HFC-23, is also a potent greenhouse gas. The secretariat of the Clean Development Mechanism estimates that a ton of HFC-23 in the atmosphere has the same effect as 11,700 tons of carbon dioxide [12].

The activity performed during this experimental master thesis is concerned to high precision spectroscopy of the ν_5 vibrational band of room-temperature CHF_3 molecule at around 8.6 μm. To increase frequency resolution of the spectroscopic measurements anon-linear saturation regime is exploited combined with the use of a single-frequency quantum cascade laser and a middle-infrared optical frequency comb.

The main goal of this spectroscopic investigation is the accurate determination with the highest precision of the main roto-vibrational absorption lines of CHF_3 to select the best spectral region for the determination of the β-ratio. Moreover, thanks to the use of the mid-infrared comb-assisted method, a full spectroscopic characterization of the roto-vibrational transition in terms of pressure line-broadening, line-shift and line saturation parameter is performed.

Finally the potential performance of a level of 10^{-12} of an optical frequency standard at 8.6 μm based on frequency-stabilized QCL laser against saturated absorption of CHF_3 is also presented.

This thesis is structured in the following way:

- **Chapter 1**
  In this chapter the main focus is on molecule absorption and its intensity profile. In particular it deals with the main causes of line broadening and shift. In the last part the non-linear absorption regime is also described.

- **Chapter 2**
  This chapter reports the main techniques that allow to overcome Doppler

broadened absorption and how to characterize them with the highest possible frequency resolution in the mid-infrared spectral region.

- **Chapter 3**
  This third chapter presents a first experimental setup for Doppler-free spectroscopy of CHF_3. Here it is characterized the performance on the system itself and it presented the collected data from a sample line with two different technique of acquisition: a direct measurement scheme and a wavelength modulation method.

- **Chapter 4**
  This last chapter presents a possible solution for the realization of a frequency standard in mid-infrared spectral region based on frequency stabilization of QCL against a sub-Doppler absorption line of CHF_3 at 8.6 μm. A detailed analysis on the frequency stability and reproducibility is also presented.

Chapter 1

Absorption

Most of our knowledge about the atomic structure of atoms comes from spectroscopic investigations. This tool is based on registration and analysis of the absorbed and emitted spectra after that an electromagnetic field had interacted with matter. Wavelength measurements of spectral lines allow to determine energy level structure, line intensity gives information, for example, about transition probability and, as consequence, the space charge distribution of electrons in atoms or about linewidth offering the possibility to understand lifetime of the involved energy levels or how the atom interact with environment (other atoms, magnetic and electric field). These are only few examples of the information that one can extrapolate from a spectroscopic investigation.

A correct model of absorption and emission phenomena is mandatory in other to extract understandable data. This first chapter deals with a brief introduction to absorption mechanism seen through different physical microscopic and macroscopic variable; after that a focus on broadening and shifting mechanism is presented in order to be able to understand line shape of absorption spectra.

1.1 Linear absorption

Assume a monochromatic electromagnetic (EM) wave with an amplitude E_0 at angular frequency ω (Fig. 1.1). In a classical representation it can be written as

$$\mathbf{E}(z,t) = \mathbf{E}_0 \cos(\omega t - kz) \tag{1.1}$$

This radiation interacts with an atom represented by a two-level system, upper level $|a>$ and lower level $|b>$, that, in a quantum mechanic description, has eigenstates at energy E_a and E_b with $E_a > E_b$ and time independent eigenfunction u_a and u_b. For wavelength $\lambda = 2\pi c/\omega \gg d$, with d dimension of considered atom, the phase of EM wave does not change much within the volume of an atom because $kz = (2\pi/\lambda)z \ll 1$ and so it is possible to neglect the spatial variation of field amplitude (dipole approximation). If the origin of the reference system is set in the center of the atom, we can set $kz \simeq 0$ so that we can rewrite 1.1

$$\mathbf{E}(z,t) = \mathbf{E}_0 \cos(\omega t) = \mathbf{A}_0(e^{iwt} + e^{-iwt}) \qquad with \quad |\mathbf{A}_0| = \frac{1}{2}\mathbf{E}_0 \tag{1.2}$$

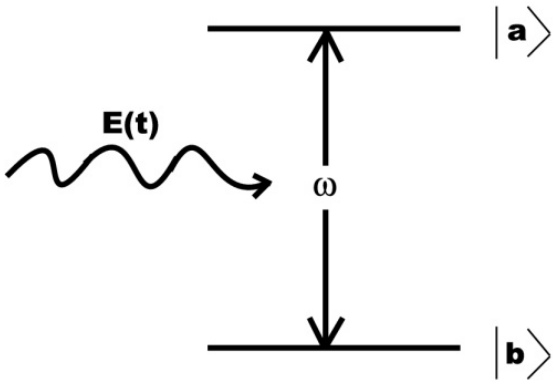

Figure 1.1: Two-level system interecting with EM field

.

The Hamiltonian operator of the atom interacting with the EM field

$$H = H_0 + V \tag{1.3}$$

can be express as a sum of an unperturbed Hamiltonian H_0 of the free atom without EM field and an operator V that takes into account the light-matter interaction. In the dipole approximation the operator V can be express

$$V = \mu \cdot \mathbf{E} = \mu \cdot \mathbf{E}_0 \cos(\omega t) \tag{1.4}$$

where $\mu = -e\mathbf{r}$ is the dipole operator..

If the interaction of EM field is weak we can use a perturbation theory to study dynamical behavior of the system, in this way we can use unperturbed atomic eigenfunctions and study rate of transitions between states. By means of Fermi Golden Rule it's possible to achieve transition rate W_{ab} between states a and b

$$W_{ab} = \frac{2\pi}{\hbar^2}|H'_{ab}|^2\delta(\omega_{ab} - \omega) \tag{1.5}$$

with

$$H'_{ab} = \int u_a^* V u_b d\tau = -\mathbf{E}\int u_a^* \mathbf{r} u_b d\tau = -\mathbf{E}\mu_{ab} \tag{1.6}$$

$\delta(\omega_{ab} - \omega)$ delta di Kronecker (different from zero when $\omega_{ab} = \omega$), $\omega_{ab} = (E_a - E_b)/\hbar$.

Matrix element H'_{ab} can be express as function of *dipole element* μ_{ab}

$$|H'_{ab}|^2 = \frac{e^2 E_0^2}{12}|\mu_{ab}|^2 \tag{1.7}$$

We can describe this interaction also as a function of the density of energy per unit volume $\rho(\omega)$, it this way we can write the transition rate of induced absorption thanks to *Einstein coefficient* of stimulated absorption B_{ab} so that

$$W_{ab} = B_{ab}\rho(\omega) \tag{1.8}$$

$$B_{ab} = \frac{\pi e^2}{3\epsilon_0 \hbar^2} |\mu_{ab}|^2 \tag{1.9}$$

with a density of energy per unit volume $\rho(\omega) = I/c$ and with $I = \frac{1}{2}\epsilon_0 c E^2$ energy flux of EM wave [13].

If we take into account that level a and b can have a sub-level structure, with $g_m\ |a_m>$ and $g_n\ |b_n>$ sub-levels, it is possible to introduce the *line strength* S_{ab}as

$$S_{ab} = \sum_{m=1}^{g_m} \sum_{n=1}^{g_n} |D_{a_m b_n}|^2 \tag{1.10}$$

In this way Einstein coefficient B_{ab} can be written in a more general formulation as

$$B_{ab} = \frac{\pi}{3\epsilon_0 \hbar} \frac{1}{g_a} S_{ab} \tag{1.11}$$

Assume an ensemble of atoms or molecules with a density per unit volume equal to N. Lower level $|b>$ has a N_b population density and upper level $|a>$ has a N_a, with $N_a + N_b = N$ and $N_a - N_b = \Delta N$.

The absorbed power per unit volume can be express through the transition rate

$$P(\omega)_{abs} = \hbar\omega W_{ab} \Delta N \tag{1.12}$$

The intensity decay of a plane EM wave propagating through a medium characterized by an *absorption coefficient* $\alpha(\omega)$ $[m^{-1}]$ is given by the LambertBeer law

$$I(\omega) = I_0 e^{\alpha(\omega) z} \tag{1.13}$$

Energy conservation required that

$$-\frac{dI}{dz} = I\alpha = P_{abs} = \hbar\omega W_{ab} \Delta N \tag{1.14}$$

$$\alpha(\omega) = \frac{2\hbar\omega W_{ab} \Delta N}{\epsilon_0 c E^2} \tag{1.15}$$

The absorption coefficient can be also obtained from the *atomic susceptibility*, in particular its imaginary part [14]:

$$\alpha(\omega) = \frac{k\chi"}{2n^2} \tag{1.16}$$

This is valid only in linear absorption regime where $\alpha(\omega)$ does not depend of incoming intensity. Non-linear absorption will be analyses in section 1.3.

Another way of describing the interaction of radiation with matter involves the definition of the *cross section parameter* σ $[m^2]$.It is expressed as units of area and represents the probability that a molecule, as a target, be hit by the incoming photon flux. The total power absorbed by the ensemble

$$P^{tot} = P_{abs} N = \sigma(\omega) I(\omega) \tag{1.17}$$

so that

$$\sigma(\omega) = \frac{\alpha(\omega)}{N} \tag{1.18}$$

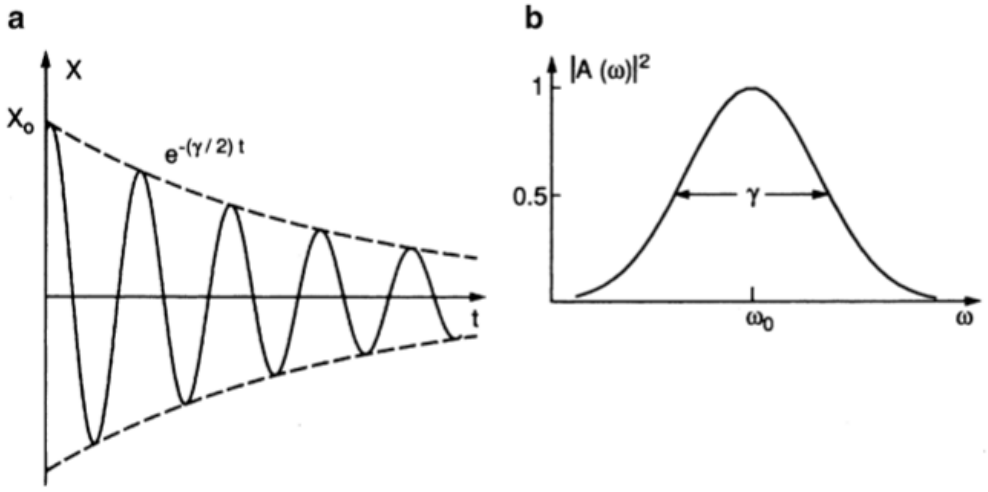

Figure 1.2: a) Damped oscillation; b) The frequency distribution of $|A(\omega)|^2$[15]

1.2 Widths and profiles of spectral lines

Spectral absorption lines are never strictly monochromatic. Even with a very high resolution interferometers, one observes a spectral distribution $I(\omega)$ around the central frequency ω of transitions. This is called *line profile*. This is due to several causes mainly divided in two classes: homogeneous broadening where all atoms/molecules manifest the same broadening, and inhomogeneous broadening where different atoms/molecules had different effect. In this chapter both these classes will be analyze in particular it will deal about natural linewidth, Doppler broadening, collisional broadening, transit time broadening.

1.2.1 Natural linewidth

An atom/molecule can emit energy as spontaneous radiation. In order to understand the spectral distribution of this kind of decay, it can be useful to introduce a classical model of a damped oscillator to describe atomic electron motion. This oscillator is define by its mass m, its force constant k and its damping factor γ.

The amplitude of the oscillation $x(t)$ can be obtain by solving its differential equation of motion

$$\ddot{x} + \gamma\dot{x} + \omega_0^2 x = 0 \tag{1.19}$$

where $\omega_0^2 = k/m$. The real solution of 1.19 with initial value $x(0) = x_0$, $\dot{x} = 0$ and a small damping parameter γ can be approximated

$$x(t) = x_0 e^{-(\gamma/2)t}\cos(\omega_0 t) \tag{1.20}$$

This is a dumped oscillation (Fig. 1.2 a) with frequency ω_0 corresponds to the central frequency of an atomic transition between E_a and E_b such that $\omega_0 = (E_a - E_b)/\hbar$. Since oscillation $x(t)$ is no longer constant but it decrees, the frequency of

the emitted radiation is no more monochromatic. Its spectral distribution can be retrieve by a Fourier transformation of $x(t)$. The amplitude $A(\omega)$ is

$$A(\omega) = \frac{1}{\sqrt{2\pi}} \int_{-\infty}^{\infty} x(t) e^{-i\omega t} \tag{1.21}$$

if $x(t) = 0$ for $t < 0$ this integral can be solved giving

$$A(\omega) = \frac{x_0}{\sqrt{8\pi}} \left(\frac{1}{i(\omega - \omega_0) + \gamma/2} + \frac{1}{i(\omega + \omega_0) + \gamma/2} \right) \tag{1.22}$$

The intensity $I(\omega) \propto A(\omega)A^*(\omega)$ (Fig 1.2 b) and in the proximity of ω_0 where $(\omega_0 - \omega)^2 \ll \omega^2$, the terms with $(\omega + \omega_0)$ can be neglect so that it's possible to retrieve the intensity profile

$$I(\omega - \omega_0) = \frac{C}{(\omega - \omega_0)^2 + (\gamma/2)^2} \tag{1.23}$$

with C a normalization constant. Setting $C = I_0\gamma/2\pi$ line profile became Lorentzian

$$L(\omega) = \frac{\gamma/2\pi}{(\omega - \omega_{ab})^2 + ()\gamma/2)^2} \tag{1.24}$$

so that

$$I(\omega - \omega_0) = I_0 L(\omega - \omega_0) \tag{1.25}$$

This line broadening can be link to the finite lifetime of energy levels. Multiplying equation 1.19 by $m\dot{x}$

$$m\ddot{x}\dot{x} + m\omega_0^2 x\dot{x} = -\gamma m\dot{x}^2 \tag{1.26}$$

Left side is time derivative of total energy W, sum of kinetic and potential energy of an armonic oscillator, and it can be written

$$\frac{d}{dt}\left(\frac{m}{2}\dot{x}^2 + \frac{m}{2}\omega^2 x^2\right) = \frac{dW}{dt} = -\gamma m\dot{x}^2 \tag{1.27}$$

Inserting $x(t)$ from equation 1.20, neglecting terms with γ^2 and time avereging we get the time-avereged radiant power P

$$P(t) = -\frac{\gamma}{2} m x_0^2 \omega_0^2 e^{-\gamma t} \tag{1.28}$$

This radiant power must be compare with the radiant power emitted by spontaneous emission. In fact an atom in exited state E_i can emit for spontaneous emission with a rate given by A_i Einstein coefficient so that given a population N_i of atoms in excite state they decay as

$$dN_i = -A_i N_i dt \tag{1.29}$$

that integrated with $N_i(0) = N_0$ become

$$N_i(t) = N_0 e^{-A_i t} \tag{1.30}$$

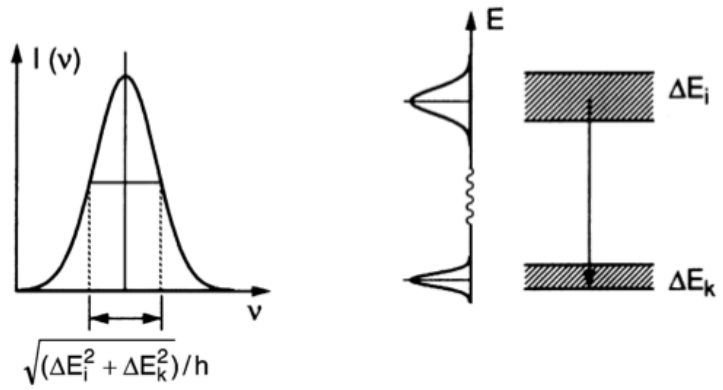

Figure 1.3: Illustration of uncertanty principle, which relates the natural linewidth to the energy uncertanties of the upper anfd lower level[15]

The radiant power P is proportional to $N(t)$

$$P(t) = N_i(t)\hbar\omega_{ab}A_i = ce^{-A_i t} \tag{1.31}$$

Comparing equation 1.28 and 1.31 we can state that natural linewidth is due to a finite lifetime of exited state with $\gamma \propto A_i$.

This can also be retrieve from the uncertainty principle (Fig. 1.3). An energy level uncertainty ΔE can be related to mean lifetime τ_i as $\Delta E_i \simeq \hbar/\tau_i$. The transition frequency $\omega_{ik} = (E_i - E_k)/\hbar$ has therefore an uncertainty

$$\delta\omega = \Delta E/\hbar = 1/\tau \tag{1.32}$$

If the lower level E_k is not in the ground state it also have a finite lifetime τ_k so that the total frequency uncertanty can be written as

$$\delta\omega_n = \sqrt{(1/\tau_i^2 + 1/\tau_k^2)} \tag{1.33}$$

1.2.2 Collisional Broadening

When two atoms A and B approach each other their energy levels shift because of interaction. In general, these shifts are different for each energy level and can be positive or negative depending on the kind of interaction (repulsive or attractive).

Typical potential curves of interaction as function of distance R between A and B are present in figure 1.4.

This interaction at distances $R < R_c$ is called *collision* and the R_c radius the *collision radius*. If no energy is transfered between the pair this collision is said *elastic*. Without any recombination mechanism the partner interact for a typical collision time $\tau_c \simeq R_c/v$, which depends on relative velocity v.

If atom A undergoes a radiative transition between energy level E_k and E_i during collision time, the frequency $\omega_{ik} = (E_i(R) - E_k(R))/\hbar$ of absorbed radiation depends on the distance $R(t)$ at time of transition.

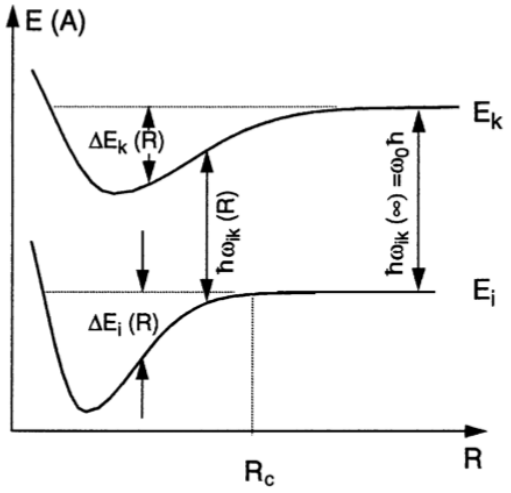

Figure 1.4: Potential curve as a function of interatomic distance R[15]

Intensity profile $I(\omega)$ of collision-broadened and shifted emission line can be obtained from

$$I(\omega) \propto \int A_{ik} P_{col}(R) \left[E_i(R) - E_k(R)\right] dR \tag{1.34}$$

where $A_{ik}(R)$ is the spontaneous transition probability, which depends on R because electronic wave function of the collision pair (AB) depends on R, and $P_{col}(R)$ is the probability per unit time that the distance between A and B lies in the range from R to $R + dR$. The probability that B has a distance between R and R+dR is proportional to $4\pi R^2 dR$ and to the Boltzmann factor $\exp\left[-V(R)/kT\right]$. The number $N(R)$ of collision partners B with a distance R from A is

$$N(R)dR = N_0 4\pi R^2 e^{-V(R)/kT} dR \tag{1.35}$$

where N_0 is the average density of molecules B.

Beside elastic collisions, inelastic collisions may also take place in which the excitation energy E_i of atom A is transfered partially or totally to atom B. Such collisions are often called *quenching collisions* because they quench the florescence by decreasing number of exited states in level E_i. It's probability A_i^{col} is

$$A_i^{col} = N_B \sigma_i \mathbf{v} \tag{1.36}$$

with

$$\mathbf{v} = \sqrt{\frac{8kT}{\pi\mu}}, \qquad \mu = \frac{M_A M_B}{M_A + M_B} \tag{1.37}$$

The total probability A_i that level E_i is depopulated is due to spontaneous emission and inelastic collision so that

$$A_i = A_i^{rad} + A_i^{coll} \tag{1.38}$$

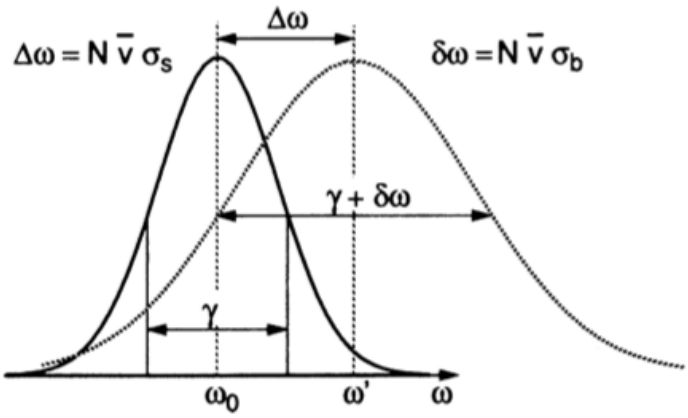

Figure 1.5: Shift and broadening of a Lorentzian line profile by collision[15]

This probability of depopulation causes a corresponding line broadening, similar to natural linewidth, keeping a Lorentzian profile, such that

$$I(\omega) = \frac{C}{(\omega - \omega_0)^2 + [(\gamma_n + \gamma_{col})/2]^2} \tag{1.39}$$

Summarizing with elastic and inelastic collision intensity profile of absorption $I(\omega)$ become

$$I(\omega) = \frac{C^*}{(\omega - \omega_0 - \delta\omega)^2 + [(\gamma_n + \gamma_{col})/2]^2} \tag{1.40}$$

with $C^* = (I_0/2\pi)(\gamma + N_B v \sigma_b)$. Line shift $\delta\omega$

$$\delta\omega = N_B v \sigma_s \tag{1.41}$$

and line broadening γ

$$\gamma = \gamma_n + N_B v \sigma_b \tag{1.42}$$

can be calculated with the number of density N_B of collision parameters B and the collision cross-section σ_s for line shift and the σ_b for broadening.

1.2.3 Transit time broadening

In transitions with a long spontaneous lifetime, e.g. rotational-vibrational transitions, the transit time $T = d/|\mathbf{v}|$ of a molecules, through a laser beam of diameter d, must be taken in consideration in broadening mechanism. Linewidth of Doppler-free molecular transitions are no longer limited by the spontaneous transition probabilities, but by the time of interaction with laser beam.

This can be seen as an harmonic oscillator that interact with Gaussian distribution of the EM field

$$E = E_0 e^{-r^2/w^2} \cos(\omega t) \tag{1.43}$$

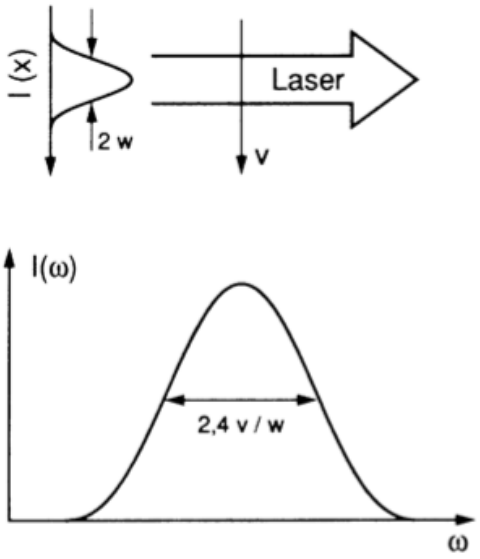

Figure 1.6: Intensity profile of an atom traversing a laser beam with a Gaussian profile with linewidth 2w[15]

where $2w$ is the diameter of the beam. Coming back to the frequency spectrum of a damped oscillator of equation 1.21 and substituting $x(t) = \alpha E$ one obtain an intensity profile

$$I(\omega) = I_0 \exp\left(-\left(\omega - \omega_0\right)^2 \frac{w^2}{2v^2}\right) \tag{1.44}$$

This is a Gaussian profile with a FWHM

$$\delta\omega_{tt} = \frac{2v}{w}\sqrt{2\ln 2} \simeq 2.4v/w \rightarrow \delta\nu_{tt} \simeq 0.4v/w \tag{1.45}$$

Until now, we have considered a plane wave front for the interacting radiation and a molecules moving parallel to these planes. However, the phase surfaces of a Gaussian beam are curved. If this effected is included in the calculation as an addition phase shift depending on the location of different molecules respect to wavefront we obtain the transit time broadened halfwidth, including the wavefront curvature effect,

$$\delta\omega = \frac{2v}{w}\sqrt{2\ln 2}\left[1 + \left(\frac{\pi w^2}{R\lambda}\right)^2\right]^{1/2} = \delta\omega_{tt}\left[1 + \left(\frac{\pi w^2}{R\lambda}\right)^2\right]^{1/2} \tag{1.46}$$

1.2.4 Doppler linewidth

In general natural linewidth can not be observed because its Lorentzian profile is concealed by other broadening effects. One of these major contribute come from Doppler width, which is due to the thermal motion of molecules.

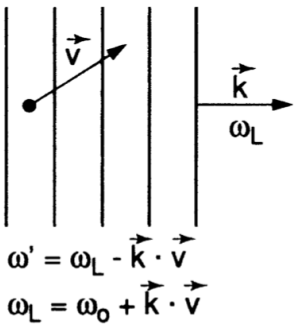

Figure 1.7: Shifted frequency due to Doppler effec. ω' frequency in molecules frame of referece; ω_L absorbed frequency[15]

Consider a molecules with a velocity $\mathbf{v}$ relative to the frame of reference of the observer. The central frequency of molecular emission ω_0 in the molecular coordinate system shifts, because of Doppler effect, to

$$\omega_e = \omega_0 + \mathbf{k} \cdot \mathbf{v} \tag{1.47}$$

where $\mathbf{k} = \frac{2\pi}{\lambda}\hat{\mathbf{u}}_k$ is the wave vector of the emitted radiation.

An observer see an increasing ω_e if molecules move towards him ($\mathbf{k} \cdot \mathbf{v} > 0$) and decreasing if molecules moves in opposite direction ($\mathbf{k} \cdot \mathbf{v} < 0$). Similarly, the frequency of a plane EM wave $\mathbf{E} = \mathbf{E_0} \exp(i(\omega t + \mathbf{k} \cdot \mathbf{r}))$ is shifted and in moving molecule frame of reference become

$$\omega^{'} = \omega - \mathbf{k} \cdot \mathbf{v} \tag{1.48}$$

Molecule can absorb only frequency $\omega^{'}$ equal to ω_0 so that the absorbed frequency $\omega = \omega_a$ (Fig. 1.7)

$$\omega_a = \omega_0 + \mathbf{k} \cdot \mathbf{v} \tag{1.49}$$

Absorption happens at higher frequency if molecules moves parallel to wave propagation. If z-direction is choose coincident with light direction so that $\mathbf{k} = \{0, 0, k_z\}$ (and $k = 2\pi/\lambda$) equation 1.49 become

$$\omega_a = \omega_0 + (1 + v_z/c) \tag{1.50}$$

At thermal equilibrium the number of molecules per unit volume $n_i(v_z)dv_z$ in level E_i with a velocity between v_z and $v_z + dv_z$ is

$$n_i(v_z)dv_z = \frac{N_i}{v_p\sqrt{\pi}} e^{-(v_z/v_p)^2} dv_z \tag{1.51}$$

where N_i is the density of the molecules in E_i level, $v_p = (2kT/m)^{1/2}$ is the most probable velocity, m is the mass of the molecule,T is absolute temperature and k is the Boltzmann constant. Using relation 1.50 for velocity v_z and frequency ω

$$n_i(\omega)d\omega = \frac{N_i c}{\omega_0 v_p \sqrt{\pi}} \exp\left[-\left(\frac{c(\omega - \omega_0)}{\omega_0 v_p} \right)^2 \right] d\omega \tag{1.52}$$

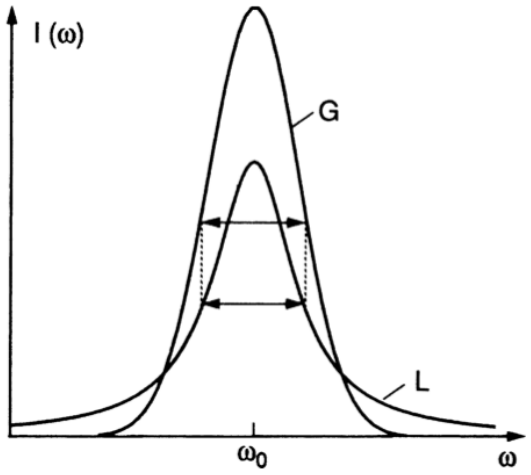

Figure 1.8: Comparison between Lorentzian and Gaussian line profiles of equal halfwidths[15]

Since absorbed power $P(\omega)d\omega$ is proportional to the density $n(\omega)d\omega$ of molecules, the intensity profile of a Doppler-broadened spectral line becomes

$$I(\omega) = I_0 \exp\left[-\left(\frac{c(\omega-\omega_0)}{\omega_0 v_p}\right)^2\right] \tag{1.53}$$

This is a Gaussian profile with a FWHM $\delta\omega_D$

$$\delta\omega_D = 2\sqrt{\ln 2}\omega_0 v_p/c = \frac{\omega_0}{c}\sqrt{8kT\ln 2/m} \tag{1.54}$$

or using mass of a mole $M = N_A m$ and gas constant $R = N_A k$ (N_A Avogadro number), in frequency unit

$$\delta\nu_D = 7.16 \times 10^{-7}\nu_0\sqrt{T/M} \tag{1.55}$$

1.2.5 Voigt profile

When different broadening contribution are present a spectral line can not be strictly represented by a Gaussian profile or by a Lorentzian profile. For example if we take into account finite lifetime of molecules and a Doppler broadening effect, not all molecules absorb at the same frequency $\omega' = \omega_0(1 + v_z/c)$. Because of the finite lifetimes of molecular energy levels, the frequency respond of these molecules is represented by a Lorentzian profile 1.25 with central frequency ω'.

Let $n(\omega')d\omega' = n(v_z)dv_z$ be the number of molecules per unit volume with velocity between v_z e $v_z + dv_z$, the spectral intensity distribution $I(\omega)$ of total absorption is then

$$I(\omega) = I_0 \int n(\omega')L(\omega-\omega')d\omega' \tag{1.56}$$

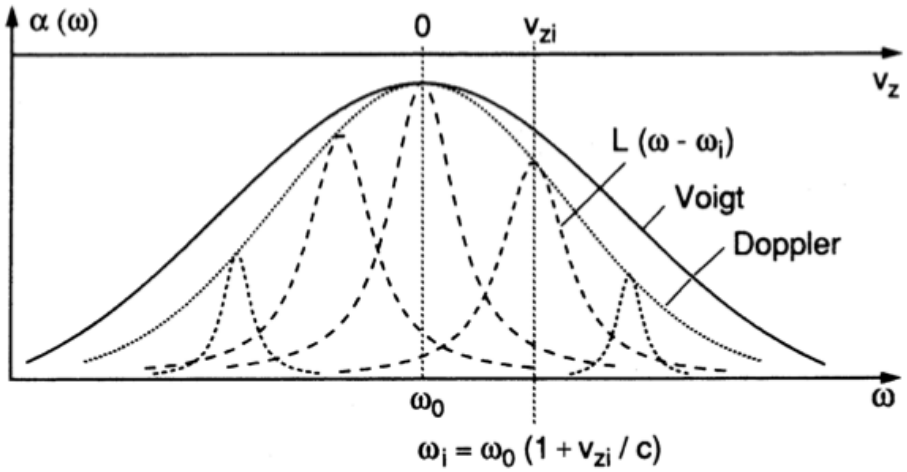

Figure 1.9: Voigt profile as a convolution of Lorentzian shape $L(\omega_0 - \omega_i)$ of molecules with different velocity component v_{zi} and central absorption frequencies $\omega_i = \omega_0(1 + v_{zi}/c)$[15]

so

$$I(\omega) = C \int_0^\infty \frac{\exp\left\{-\left[(c/v_p)\left(\omega_0 - \omega'\right)/\omega_0\right]^2\right\}}{\left(\omega - \omega'\right)^2 + (\gamma/2)^2} d\omega' \tag{1.57}$$

with

$$C = \frac{\gamma N_i c}{2 v_p \pi^{3/2} \omega_0} \tag{1.58}$$

This intensity profile, which is a convolution of Lorentzian and Gaussian profile, is called *Voigt profile* (Fig. 1.9).

1.3 Non-linear absorption

At sufficiently large laser intensities, the pumping rate becomes higher than the relaxation rates resulting in a decrease of the population in absorbing level. This result in a nonlinear dependence, a saturation, of the absorbed radiation power on the incident power. In the following section the basic physics of nonlinear absorption is discussed. The spectral profile of such partially saturated transition are different for homogeneous and inhomogeneous broadened line so they will be treated separately.

1.3.1 Saturation of level population

Consider a 2 level system with population densities N_1 and N_2 of respective levels. This two levels are coupled each other by absorption and emission processes as shown in figure 1.10.

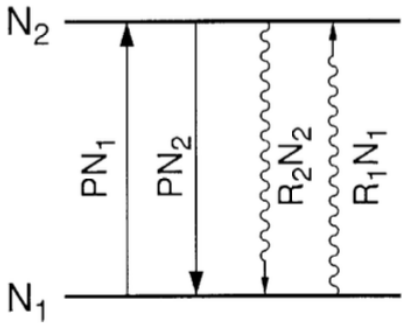

Figure 1.10: Two level system with pumping and relaxing processes[15]

With probability $P = B_{12}\rho(\omega)$ for transition $|1> \rightarrow |2>$ by absorption of a photon $\hbar\omega$ and relaxation probability R_i for level $|i>$, the rate equation for population densities is

$$\frac{dN_1}{dt} = -\frac{dN_2}{dt} = -PN_1 - R_1N_1 + PN_2 + R_2N_2 \tag{1.59}$$

At the stationary regime ($dN_i/dt = 0$) we obtain with $N = N_1 + N_2$

$$(P + R_1)N_1 = (P + R_2)(N - N_1) \Rightarrow N_1 = N\frac{P + R_2}{2P + R_1 + R_2} \tag{1.60a}$$

$$(P + R_2)N_2 = (P + R_1)(N - N_2) \Rightarrow N_2 = N\frac{P + R_1}{2P + R_1 + R_2} \tag{1.60b}$$

For high pumping rate ($P \rightarrow \infty$), populations approach to $N/2$ so that absorption coefficient $\alpha = \sigma(N_1 - N2)$ approaches zero.

Without any pumping mechanism ($P = 0$) the population densities are

$$N_{10} = \frac{R_2}{R_1 + R_2}N, \qquad N_{20} = \frac{R_1}{R_1 + R_2}N \tag{1.61}$$

With $\Delta N = N_1 - N_2$ and $\Delta N_0 = N_{10} - N_{20}$ we could write

$$\Delta N = N\frac{R_2 - R_1}{2P + R_1 + R_2} \tag{1.62a}$$

$$\Delta N_0 = N\frac{R_2 - R_1}{R_1 + R_2} \tag{1.62b}$$

which gives

$$\Delta N = \frac{\Delta N_0}{1 + 2P/(R_1 + R_2)} = \frac{\Delta N_0}{1 + S} \tag{1.63}$$

The *saturation parameter*

$$S = \frac{2P}{(R_1 + R_2)} = \frac{P}{\overline{R}} \tag{1.64}$$

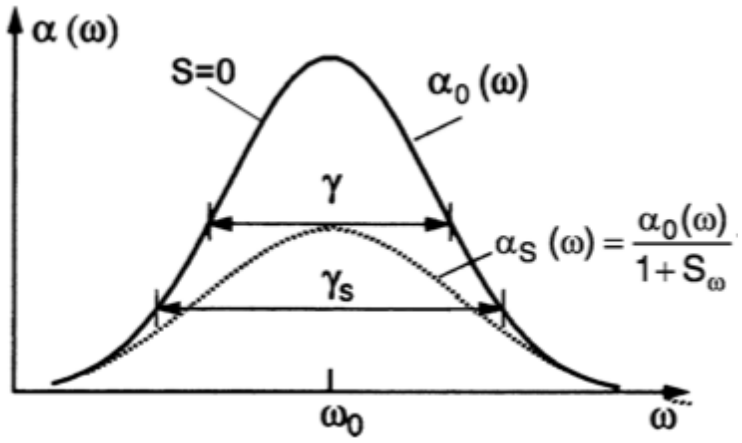

Figure 1.11: Saturation broadening of a homogeneous line profile[15]

represents the ratio between pumping rate P and the average relaxation rate $\overline{R} = (R_1 + R_2)/2$. We can also calculate the saturated absorption coefficient $\alpha(\omega) = \sigma_{12}\Delta N$

$$\alpha = \frac{\alpha_0}{1+S} \tag{1.65}$$

being α_0 the unsaturated absorption coefficient without pumping.

1.3.2 Saturation of homogeneous line profiles

According to equation 1.12 the power absorbed per unit volume on transition $|1> \rightarrow |2>$ by atoms with population densities N_1 e N_2 in a radiation field with a spectral energy density $\rho(\omega)$ is

$$P = \hbar\omega B_{12}\rho(\omega)\Delta N = \hbar\omega B_{12}\rho(\omega)\frac{\Delta N_0}{1+S} = \hbar\omega\overline{R}\frac{\Delta N_0}{1+S^{-1}} \tag{1.66}$$

with $S = B_{12}\rho(\omega)/\overline{R}$.

We can also introduce a frequency dependent saturation parameter S_ω, in order to taking into account the Lorentzian profile of absorption probabilities, so that

$$S_\omega = \frac{B_{12}\rho(\omega)}{\overline{R}}L(\omega-\omega_0) = S_0\frac{(\gamma/2)^2}{(\omega-\omega_0)^2+(\gamma/2)^2} \tag{1.67}$$

with $S_0 = S(\omega_0)$. Substituting in equation 1.66 we obtain

$$P(\omega) = \frac{\hbar\omega\overline{R}\Delta N_0 S_0(\gamma/2)^2}{(\omega-\omega_0)^2+(\gamma/2)^2(1+S_0)} = \frac{C}{(\omega-\omega_0)^2+(\gamma_s/2)^2} \tag{1.68}$$

This is again a Lorentzian profile but with an increased FWHM $\gamma_s = \gamma\sqrt{1+S_0}$.

From equation 1.68 is possible to retrieve the absorption coefficient α

$$\alpha_s(\omega) = \alpha_0(\omega_0)\frac{(\gamma/2)^2}{(\omega-\omega_0)^2+(\gamma_s/2)^2} = \frac{\alpha_0(\omega)}{1+S_\omega} \tag{1.69}$$

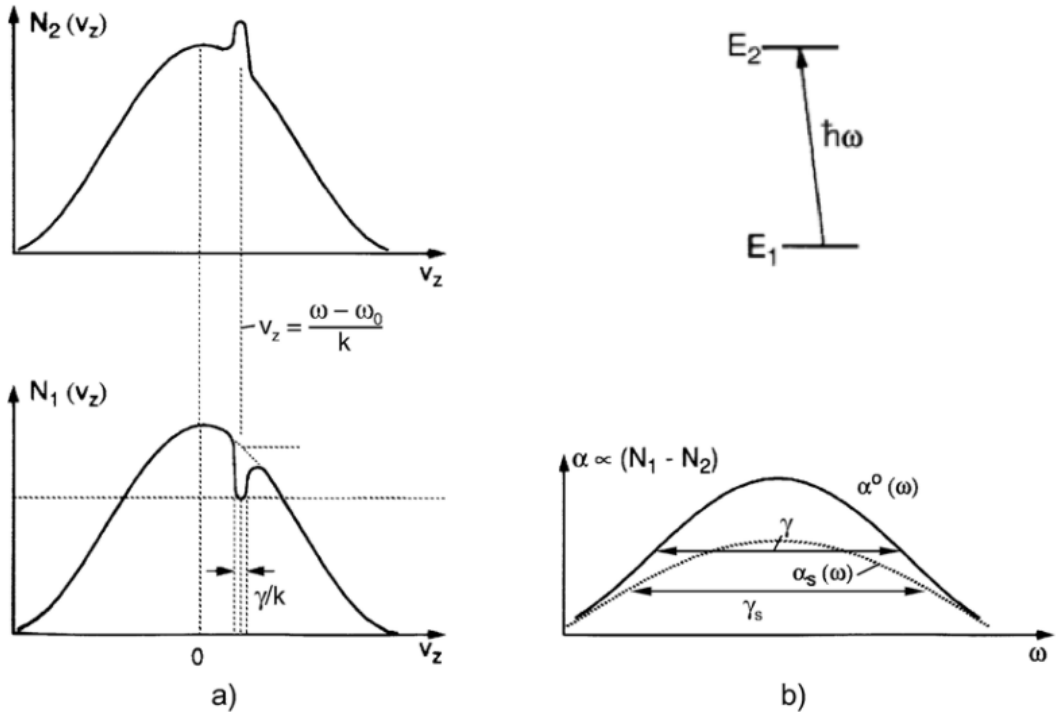

Figure 1.12: Velocity-selective saturation of a Doppler-broadened transition: a) Bennet hole in the lower and Bennet dip in the upper state population distribution $N_i(v_z)$; b) Saturated absorption profile (dashed curve) when the saturation laser is tuned across the Doppler profile of a molecular transition[15]

where

$$\alpha_0(\omega) = \frac{\alpha_0(\omega_0)(\gamma/2)^2}{(\omega-\omega_0)^2+(\gamma/2)^2}; \qquad \alpha_0(\omega_0) = \frac{2\hbar\omega B_{12}\Delta N_0}{\pi c\gamma} \tag{1.70}$$

This shows that the saturation decreases the absorption coefficient by $(1 + S_\omega)$ factor. At line center, this factor has its maximum value so that saturation is stronger; at line wing saturation is weaker. This effect brings to a line broadening.

1.3.3 Saturation of inhomogeneous line profiles

The absorption cross-section for a molecule with a Maxwell-Boltzmann distribution of velocity around v_z through a monochromatic light wave $E = E_0\cos(\omega t+kz)$ without saturation can be written as

$$\sigma_{12} = \sigma_0\frac{(\gamma/2)^2}{(\omega-\omega_0-kz)^2+(\gamma/2)^2} \tag{1.71}$$

where $\sigma_0 = \sigma(\omega = \omega_0 + kz)$ is the maximum cross section at the line center of Doppler-shifted molecular transition and γ natural linewidth of transition.

Due to saturation, density of population of levels changes: while lower level $|1>$ with density $N_1(v_z)dv_z$ decreases in velocity interval $dv_z = \gamma/K$, upper level $|2>$ with density $N_2(v_z)dv_z$ increases correspondingly.

With equation 1.63 and 1.67 it possible to write the new population densities of level $|1>$ and $|2>$ as

$$N_1(\omega, v_z) = N_0^1(v_z) - \frac{\Delta N^0}{\gamma_1 \tau}\left[\frac{S_0(\gamma/2)^2}{(\omega-\omega_0-kz)^2+(\gamma_s/2)^2}\right] \tag{1.72a}$$

$$N_2(\omega, v_z) = N_0^2(v_z) + \frac{\Delta N^0}{\gamma_2 \tau}\left[\frac{S_0(\gamma/2)^2}{(\omega-\omega_0-kz)^2+(\gamma_s/2)^2}\right] \tag{1.72b}$$

where $\gamma = \gamma_1 + \gamma_2$ denotes the homogeneous width of transition and $\gamma_s = \gamma\sqrt{1+S_0}$ (Fig. 1.12 a). The quantity

$$\tau = \frac{1}{\gamma_1} + \frac{1}{\gamma_2} = \frac{\gamma}{\gamma_1\gamma_2} \tag{1.72c}$$

is called the *longitudinal relaxation time* and

$$T = \frac{1}{\gamma_1+\gamma_2} = \frac{1}{\gamma} \tag{1.72d}$$

is the *transverse relaxation time*.

Subtracting (1.72b) from (1.72a) yields for the saturated population difference

$$\Delta N(\omega_s, v_z) = \Delta N^0(v_z)\left[1 - \frac{S_0(\gamma/2)^2}{(\omega-\omega_0-kz)^2+(\gamma_s/2)^2}\right] \tag{1.73}$$

This distribution presents a minimum at $v_z = (\omega-\omega_0)/k$ which is called *Bennet hole* (Fig 1.12 a). This hole has an homogeneous width $\gamma_s = \gamma\sqrt{1+S_0}$ and a depth at the center $\Delta N_0 S_0/(1+S_0)$.

The total absorption coefficient can be calculated

$$\alpha(\omega) = \int \Delta N(v_z)\sigma_{12}(\omega, v_z)dv_z \tag{1.74}$$

Using $\Delta N v_z$ from (1.73), σ_{12} from (1.71) and $\Delta N^0(v_z)$ from (1.51) yields

$$\alpha(\omega) = \frac{\Delta N \sigma_0}{v_p\sqrt{\pi}} \int \frac{e^{-(v_z/v_p)^2}dv_z}{(\omega-\omega_0-kz)^2+(\gamma_s/2)^2} \tag{1.75}$$

that, despite saturation effect is again a Voigt profile but with a different amplitude and linewidth (from γ to γ_s) (Fig. 1.12 b).

Integral (1.75) can be approximated taking into account that Doppler profile is much larger than homogeneous width γ_s so that numerator does not vary much in the interval $\Delta v_z = \gamma_s/k$. Therefore we can take out the exponential from integral and solved with $v_z = (\omega-\omega_0)/k$

$$\alpha_s(\omega) = \frac{\alpha^0(\omega_0)}{\sqrt{1+S_0}} \exp\left\{-\left[\frac{\omega-\omega_0}{0.6\delta\omega_D}\right]^2\right\} \tag{1.76}$$

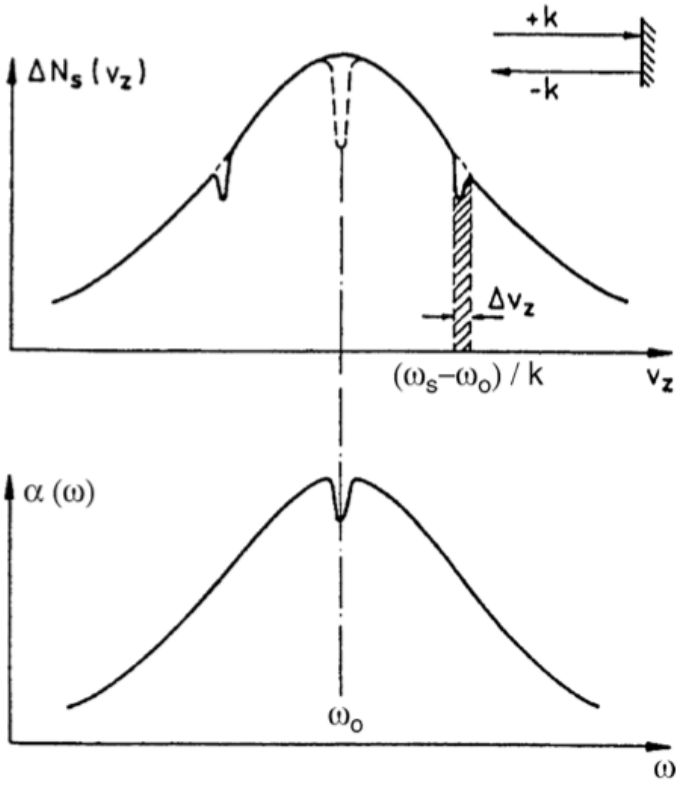

Figure 1.13: Bennet holes caused by the two counter-propagating waves for $\omega \neq \omega_0$ and $\omega = \omega_0$ (dashed curve). Lamb dip in absorption profile[15]

with the unsaturated absorption coefficient

$$\alpha_0(\omega_0) = \Delta N_0 \frac{\sigma_0 \gamma c \sqrt{\pi}}{v_p \omega_0}$$

and Doppler width

$$\delta\omega_D = \frac{\omega_0}{c}\sqrt{\frac{8kT\ln 2}{m}}$$

Bennet holes can not be directly detected; however it is possible to observe them if two laser beams are used. The first pump laser burns a hole into the population density whereas the second one, a weak probe laser, scans the created hole. It is possible to use the same laser for pump and probe if the incident beam is reflected back into the sample (Fig. 1.13).

If the intensity of the retro-reflect beam is weak respect the incoming one, absorption coefficient can be express

$$\alpha_s(\omega) = \alpha^0(\omega)\left[1 - \left(1 + \frac{S_0}{2}\frac{(\gamma_s/2)^2}{(\omega-\omega_0)^2 + (\Gamma_s^*/2)^2}\right)\right] \tag{1.77}$$

This represent a Lorentzian saturation profile burned at the frequency ω_0 with a FWHM equal to $\Gamma_s^* = (\gamma + \gamma_s)/2 = (\gamma + \gamma\sqrt{1+S_0})/2$. This is called *Lamb dip*.

1.4 CHF_3 around 8.6 μm

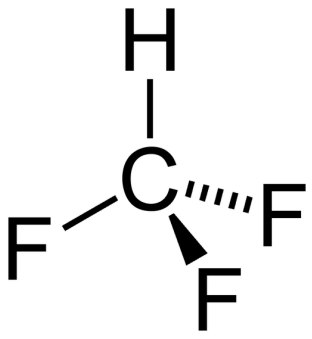

Figure 1.14: Strurcture of Fluoroform molecule

Fluoroform is the chemical compound with the formula CHF_3. It is one of the "haloforms", a class of compounds with the formula CHX_3 (X = halogen). Fluoroform is used in diverse niche applications and is produced as a by-product of the manufacture of Teflon. It is also generated biologically in small amounts apparently by decarboxylation of trifluoroacetic acid. in addiction, CHF_3 is used in the semiconductor industry in plasma etching of silicon oxide and silicon nitride. Known as R-23 or HFC-23, it is also a useful refrigerant, sometimes as a replacement for chlorotrifluoromethane (cfc-13) and is a byproduct of its manufacture. Moreover, CHF_3 is also a potent greenhouse gas. The secretariat of the Clean Development Mechanism estimates that a ton of HFC-23 in the atmosphere has the same effect as 11,700 tons of carbon dioxide [12].

This molecule has been selected in order to investigate proton-to-electron mass ratio, $\beta = m_p/m_e$, which characterizes the strength of strong interaction in terms of the electro-weak one. This can be done by measure the frequency ν_{vib} of a given molecular ro-vibrational transition relative to the clock hyperfine transition ν_{hyp} in the Cs electronic ground state ($|F = 4; m_F = 0 > \leftrightarrow |F = 3; m_F = 0 >$) [11]. To enhance the spectroscopic interrogation time, which sets the ultimate resolution achievable in a single measurement, a Ramsey-fringes technique will be adopted [16]. In this scheme one first wants to minimize the fringe periodicity P, given by the ratio of the mean longitudinal speed of the molecules in the beam, to enlarge fringe contrast, which can be accomplished by reducing the velocity dispersion, and to have a low rotational temperature. A two-photon spectroscopy is perform with a molecular beam with intense flux, low temperature, and reduced longitudinal speed. This will be attained by combining buffer-gas cooling and Stark manipulation. Since buffer-gas cooling operates with nearly all species, potentially any molecule with a relatively high electric dipole moment (EDM) and a favorable two-photon transition may be chosen for the experiment. The CHF_3 molecule exhibits both these features.

The main vibrational mode of this molecule are These are ν_1 (CH symmetric-stretching) at 3025 cm^{-1}, ν_2 (CF_3 symmetric-stretching) at 1141 cm^{-1}, ν_3 (CF_3

symmetric-deformation) at 700 cm^{-1}, ν_4 (CH bending) at 1377 cm^{-1}, ν_5 (CF_3 asymmetric-stretching) at 1152 cm^{-1}, ν_6 (CF_3 asymmetric-deformation) at 508 cm^{-1}.

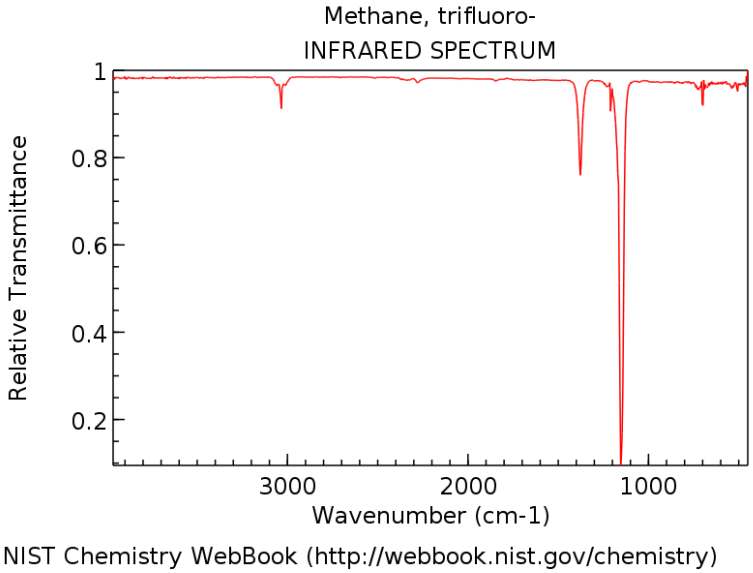

Figure 1.15: Infrared spectrum of CHF_3

The infrared spectrum of CHF_3 is shown in Fig 1.15. We can clearly distinguish 4 main vibrational transition band.

We will focus our analysis from 1155 cm^{-1} to 1160 cm^{-1} (frequency available from our QCL source) where we can find an absorption around 1158.75 cm^{-1}. This transition has been select as a two photon transition for the Ramsey interrogation [11].

This spectral region is very dense of absorption line due to the various roto-vibrational transition.

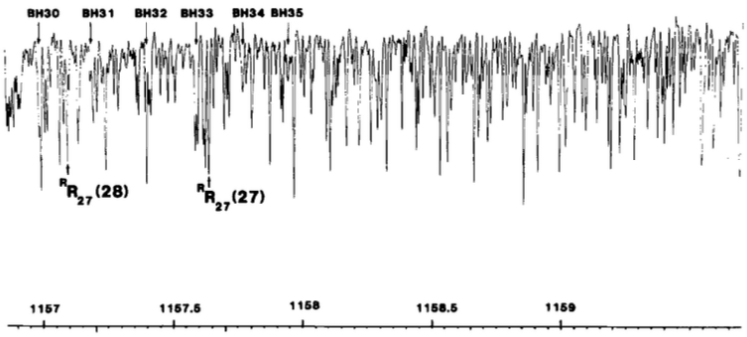

Figure 1.16: Fourier transform experimental spectrum (p=0.002tor, L=32,17m) around 1158 cm^{-1}. [17]

Chapter 2

MIR Precision Spectroscopy

As already explained in the previous chapter, the absolute measurement of the line-center frequency of an atomic/molecular transition is limited by broadening mechanisms. Even natural linewidth is difficult to observe because it is surrounded by other effect, especially Doppler broadened width. Some spectroscopy technique have been developed in order to overcome this limitation. Besides that, it is necessary to set up a system to sense and absolute measure this sub-Doppler transition line. Laser pump and probe beams should have an emission line narrower than the scanned absorption line and their frequency should be know with high precision.

This chapter deals with this problem. It introduces Doppler-free spectroscopy to overcome broadening effect, a frequency modulation method to sense with an high sensitivity sub-Doppler line and an absolute frequency measure through an optical frequency comb synthesizer(OFCS).

2.1 Doppler-free spectroscopy

Doppler-free spectroscopy, called also saturation spectroscopy, is a spectroscopic method able to cancel the contribute (first order) of the Doppler broadening. This kind of measurement gain one/two order of magnitude in sensing different transitions. In fact, in the case of a gas sample, Doppler width is much lager than other effect, e.g. collisional broadening, and can include within the same Doppler profile more than one transition. Through saturation effect it is possible to make measurable these sub-Doppler lines in order to identify with high precision these transitions which, otherwise can not be detected.

As described in the previous chapter a simple Doppler-free spectroscopic method is based on the pump and probe configuration. Pump beam should be enough intense to produce non-linear effect and burn hole into population density of state of transition; it select a specific class of the velocity distribution. Probe laser, instead, has to sense the difference between population, but, it should not be much intense in order to prevent other modification of states.

Among the different implementation of pump-probe spectroscopic setups, one of the simplest exploits the same laser beam for pump and probe by retro-reflexing

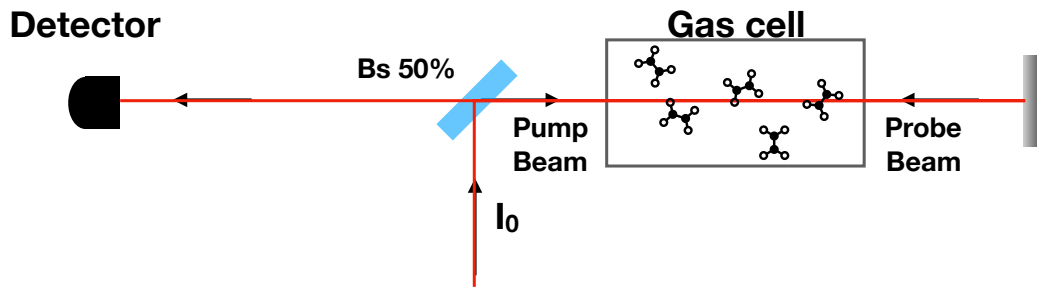

Figure 2.1: Schematic setup for Lamb dip detection with same laser beam for pump and probe

the incident beam back into the a sample. Fig.2.1

In this case pump beam and probe beam has the same intensity and frequency but different and opposite wavevectors. In this standing wave situation population difference due to saturation is

$$\Delta N(v_z) = \Delta N^0(v_z)\left[1 - \frac{S_0(\gamma/2)^2}{(\omega_0 - \omega - kv_z)^2 + (\gamma_s/2)^2} - \frac{S_0(\gamma/2)^2}{(\omega_0 - \omega + kv_z)^2 + (\gamma_s/2)^2}\right] \tag{2.1}$$

where S_0 is saturation parameter due to $I = I_1 = I_2$. Because of opposite Doppler shift two Bennet holes are created at velocity components $v_z = \pm(\omega_0 - \omega)/k$.

The saturated absorption coefficient becomes

$$\alpha_s(\omega) = \int \Delta N(v_z)\left[\sigma(\omega_0 - \omega - kv_z) + \omega_0 - \omega + kv_z)\right] dv_z \tag{2.2}$$

Using equation (1.71) and (2.1) it's possible to retrieve, in the approximation $S_0 \ll 1$ the saturated-absorption coefficient for a sample in standing wave field

$$\alpha_s(\omega) = \alpha^0(\omega)\left[1 - \frac{S_0}{2}\left(1 + \frac{(\gamma_s/2)^2}{(\omega - \omega_0)^2 + (\gamma_s/2)^2}\right)\right] \tag{2.3}$$

with $\gamma_s = \gamma\sqrt{1 + S_0}$ and $S_0 = S(I, \omega_0)$.

This represent the Doppler-broadened absorption profile $\alpha^0(\omega)$ with a dip at the line center $\omega = \omega_0$, which is called Lamb dip (Fig 2.2). For $\omega = \omega_0$ the saturated absorption coefficient is $\alpha(\omega_0) = \alpha^0(\omega_0)(1 - S_0)$ with $S_0 = B_{ik}I/c\gamma_s$. For $(\omega - \omega_0) \gg \gamma_s$ the saturated absorption coefficient is $\alpha(\omega_0) = \alpha^0(\omega_0)(1 - S_0/2)$.

If retro-reflected probe beam has an intensity $I_2 \ll I_1$ we obtain a similar result but $\Gamma_s^* = (\gamma_s + \gamma)/2$ must be substituted in order to obtain

$$\alpha_s(\omega) = \alpha^0(\omega)\left[1 - \frac{S_0}{2}\left(1 + \frac{(\gamma_s/2)^2}{(\omega - \omega_0)^2 + (\Gamma_s^*/2)^2}\right)\right] \tag{2.4}$$

Fig. 2.2 shows Lamb dip for different saturation parameter S.

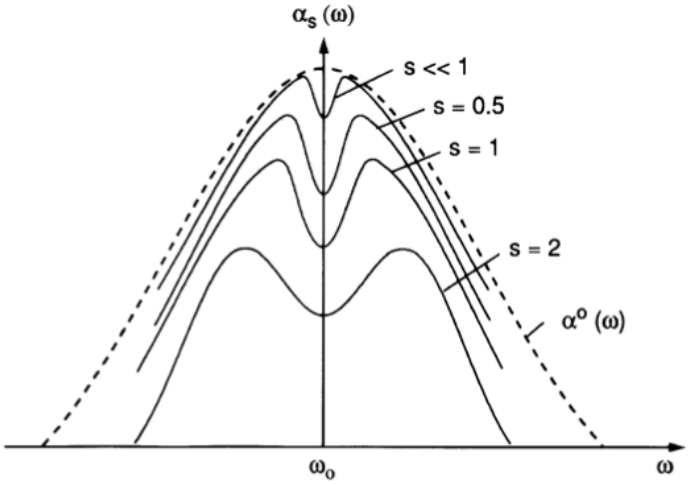

Figure 2.2: Lamb dips for different saturation parameter S_0[15]

2.2 Wavelength modulation spectroscopy

The sensitivity of direct absorption spectrometry is ultimately limited by technical noise in both laser intensity and photodetectors, which has $1/f$ dependence (flicker noise). In order to reduce the noise is enough to shift detection to higher frequency and this can be done by modulation techniques. When modulated light is sent through a sample, the information about the analyte is encoded at the modulation frequency (and its overtones) and later retrieved by a synchronous demodulation of the detected signal. In frequency modulation spectrometry (FMS) the modulation frequency is in the RF range, of the same order of magnitude as the width of the probed transition, while in wavelength modulation spectrometry (WMS) the modulation is slower (at an audio frequency), while instead the amplitude is in the range of the transition width.

In both the modulation schemes the laser frequency ω_0 is modulated at a frequency Ω which change ω_0 periodically from $\omega_0 - \Delta\omega_L/2$ to $\omega_0 + \Delta\omega_L/2$. After laser pass through the sample, absorption and dispersion profiles of the optical resonance convert the frequency modulation in an amplitude modulation that can be detected by a lock-in amplifier (phase sensitive detector) tuned to modulation frequency Ω. This correspond to detect the difference $\Delta P_\Gamma = P_\Gamma(\omega_L - \Delta\omega_L/2) - P_\Gamma(\omega_L + \Delta\omega_L/2)$. For small $\Delta\omega_L$, it can be expand in Taylor series.

$$\Delta P_\Gamma(\omega) = \frac{dP_\Gamma}{d\omega}\Delta\omega_L + \frac{1}{2!}\frac{d^2P_\Gamma}{d\omega^2}\Delta\omega_L^2 + \dots \tag{2.5}$$

The first term is dominant and it is proportion to the first derivative of absorption spectrum $\alpha(\omega)$, in fact

$$\frac{d\alpha(\omega)}{d\omega} = -\frac{1}{P_0 L}\frac{dP_\Gamma}{d\omega} \tag{2.6}$$

If laser frequency is sinusoidally modulated, $\omega_L = \omega_0 + \frac{\Delta\omega_L}{2}\sin\Omega t$, the Taylor

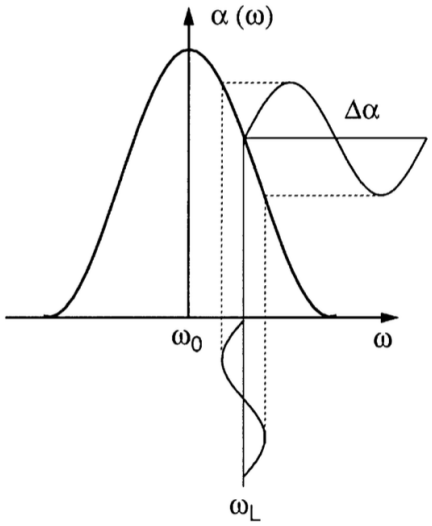

Figure 2.3: Graphical representation of wavelength modulation technique

expansion become,

$$P_\Gamma(\omega_L) = P_\Gamma(\omega_0) + \sum_n \frac{\alpha^n}{n!} \sin^n \Omega t \left(\frac{d^n P_\Gamma}{d\omega^n}\right) \tag{2.7}$$

For $\alpha L \ll 1$ it is possible to write

$$\left(\frac{d^n P_\Gamma}{d\omega^n}\right)_{\omega=\omega_0} = -P_0 x \left(\frac{d^n \alpha(\omega)}{d\omega^n}\right)_{\omega=\omega_0} \tag{2.8}$$

Inserting in equation (2.7) and collecting isofrequency terms

$$\begin{aligned}
\frac{\Delta P_\Gamma}{P_0} = -\alpha L \left[\frac{a}{4}\left(\frac{d^2\alpha}{d\omega^2}\right)_{\omega_0} + \frac{a^3}{64}\left(\frac{d^4\alpha}{d\omega^4}\right)_{\omega_0} + \ldots\right] + \\
+ \left[\left(\frac{d\alpha}{d\omega}\right)_{\omega_0} + \frac{a^2}{8}\left(\frac{d^3\alpha}{d\omega^3}\right)_{\omega_0} + \ldots\right] \sin(\Omega t) + \\
+ \left[-\frac{a}{4}\left(\frac{d^2\alpha}{d\omega^2}\right)_{\omega_0} + \frac{a^3}{48}\left(\frac{d^4\alpha}{d\omega^4}\right)_{\omega_0} + \ldots\right] \cos(2\Omega t) + \\
+ \left[\frac{a^2}{24}\left(\frac{d^3\alpha}{d\omega^3}\right)_{\omega_0} + \frac{a^4}{384}\left(\frac{d^5\alpha}{d\omega^5}\right)_{\omega_0} + \ldots\right] \sin(3\Omega t) + \\
+ \ldots
\end{aligned}$$

For small modulation amplitude $d_A = \Delta\omega_L/\Delta\omega_x \ll 1$, with $\Delta\omega_x$ linewidth of probed transition, the first terms in each bracket are dominant. So we can write the signal $S(n\Omega)$ for each harmonic of modulation frequency Ω. In particular, the

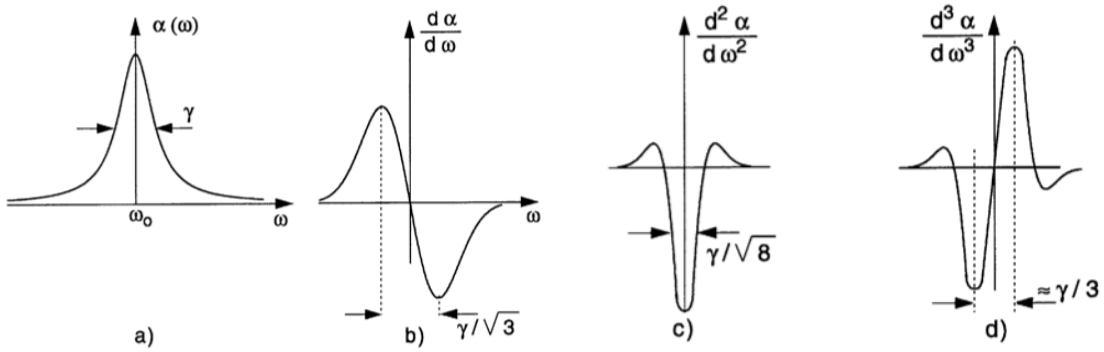

Figure 2.4: Lorentzian profile $\alpha(\omega)$ (a) with first (b), second (c) and third (d) derivative

signals for the first three derivatives of the absorption coefficient $\alpha(\omega)$, shown in Fig. 2.4, are

$$S(\Omega) = -\alpha L \frac{d\alpha}{d\omega} \sin(\Omega t) \tag{2.9a}$$

$$S(2\Omega) = +\frac{\alpha^2}{4} L \frac{d^2\alpha}{d\omega^2} \cos(2\Omega t) \tag{2.9b}$$

$$S(3\Omega) = +\frac{\alpha^3}{24} L \frac{d^3\alpha}{d\omega^3} \sin(3\Omega t) \tag{2.9c}$$

For increasing modulation amplitude, but still with $d_A < 1$, also the signal $S(n\Omega)$ is increasing. For $d_A > 1$ this is no more valid and the signal $S(n\Omega)$ starts to deform. Fig. 2.5 shows how $A_1 = S(\Omega)$ and $A_3 = S(3\Omega)$ modify for increasing d_A ratio. For example $S(\Omega)$ shows the maximum peak to peak signal for $d_A = 1.8$ but the maximum slope at around the line center is observed for $d_A = 1$.

Frequency modulation of a laser source can be obtained in different ways. For example by periodically changing the cavity length d (by mounting a cavity mirror on a piezo) by means of an external frequency modulator (either electro- or acoustic-optic modulator) or, in the case of a semiconductor laser, simply by modulating the injected pump current.

2.3 Absolute frequency measurement

Frequency can by far be measured with the highest precision of all physical quantities. In the radio frequency (rf) domain (say up to 100 GHz), electronics frequency counters are routinely employed for a long time. Almost any of the most precise measurements in physics have been performed with such a counter that uses an atomic clock as a time base. To extend this accurate technique to higher frequencies, so called harmonic frequency chains have been constructed since the late 1960s [19]. In such a chain, nonlinear elements produce frequency multiples (harmonics) of a given oscillator to which a subsequent oscillator is phase locked.

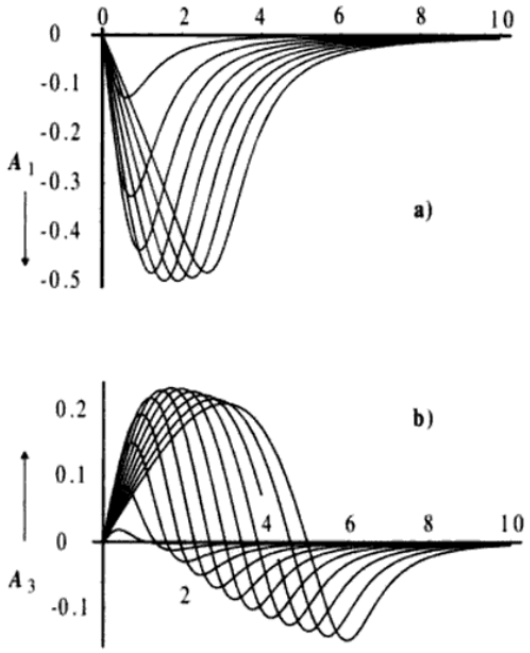

Figure 2.5: Amplitude of the first and third harmonic of demodulate signal for increasing modulation parameter (d_A= 0.2,0.6,1.0,...,3.0 for A_1 ; d_A= 0.5,1.0,1.5,...,6.0 for A_3) [18]

Repeating the multiplication and phase-lock procedure many times makes it possible to convert a reference radio frequency, say from an atomic clock, to much higher frequencies. Because of the large number of steps necessary to build a long harmonic frequency chain, it was not before 1995 when visible laser light was first referenced phase coherently to a cesium atomic clock using this method [20]. The disadvantage of these harmonic frequency chains was not only that they could easily fill several large laser laboratories at one time, but that they could be used to measure only a single optical frequency. Even though mode-locked lasers for optical frequency measurements were used in rudimentary form in the late 1970s [21], this method did not become practical until the advent of femtosecond (fs) mode-locked lasers and the invention of the optical frequency comb synthesizer. [22]

2.3.1 Optical frequency comb synthesizer

A mode-locking laser creates optical pulse trains with a certain periodicity T_r that is related to cavity length L, through the effective refraction index n and speed of light c as

$$T_R = \frac{2nL}{c} \tag{2.10}$$

Figure 2.6.a shows the electric field of the generated pulse trains as a function of time.

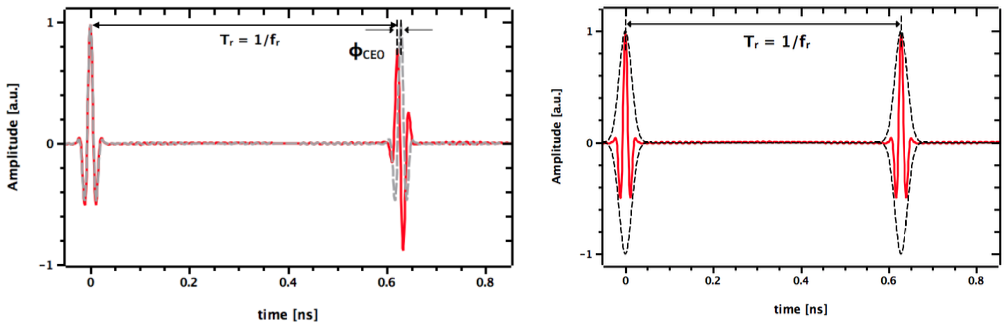

(a) *(b)*

Figure 2.6: a) Frequency comb output pulse electric field (red) and envelope (black dashed). b)Frequency comb ideal pulse output (red) and real with a phase offset (grey shaded).

The red continuous curve represents the optical electric field intensity emitted by the laser while the black dashed curve is the envelope. In the case where the cavity and material dispersion are fully compensated the output pulse duration is said to be transform limited and is directly related to the optical spectrum by:

$$\Delta\tau = \frac{k}{\Delta\nu} \tag{2.11}$$

where k is the time-bandwidth product whose value depends on the pulse shape and $\delta\nu$ is the optical spectrum bandwidth.

In the spectral domain the same periodic structure appears with a tooth separation of f_{rep} called *repetition rate* and which is precisely the free spectral range (FSR) of the laser cavity Fig 2.7.

$$f_{rep} = \frac{1}{T_r} \tag{2.12}$$

The optical spectrum is mainly given by the active medium emission spectra and its non linear effects. The FWHM gives the spectrum bandwidth $\Delta\nu$.

A more realistic pulse train is depicted in 2.6.b where the dashed grey curve represents the ideal case while the red line is the more accurate electric field behaviour. The periodicity is the same as before while the pulse peak appears as moving in position from pulse to pulse. The phase difference between the ideal and real peak position is called the Carrier Envelope Offset phase, ϕ_{CEO}, and is related to the more useful frequency parameter ν_{CEO} by:

$$\nu_{CEO} = \frac{\phi_{CEO}}{2\pi T_r} \tag{2.13}$$

This phenomena is explained by the difference between the group v_g and phase v_p velocities in the laser cavity that give rise to the phase slipping between the carrier frequency electric field and the envelope profile. ϕ_{CEO} can be express ad

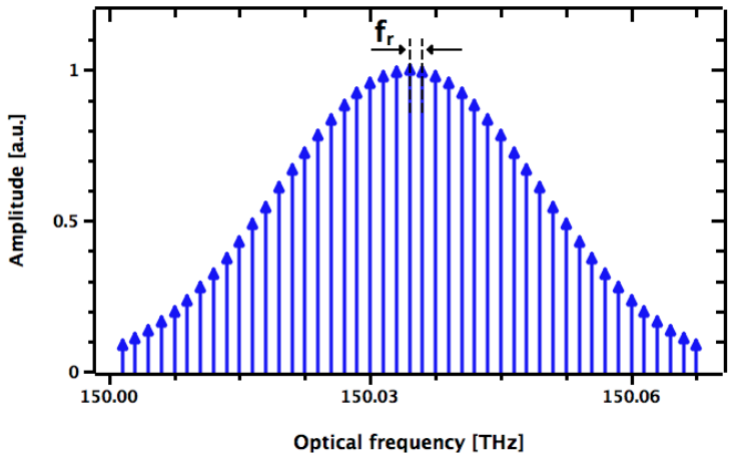

Figure 2.7: Frequency comb spectrum

the sum of two contribution: a static offset ϕ_0 and $\Delta\phi_{CEO}$ represents the pulse-to-pulse change in carrier envelope phase due to conditions inside the cavity of the laser oscillator.

$$\phi_{CEO} = \phi_0 + \Delta\phi_{CEO} \tag{2.14}$$

As the pulse propagates through any medium outside the laser cavity (except vacuum), a difference between the phase and group velocities (caused by dispersion) will cause ϕ_0 to vary; so in reality,ϕ_0 is not truly static. In a similar vein, the physical origin of ϕ_{CEO} results from dispersion of the optical elements inside a laser cavity. In the case of ϕ_0, the pulse is sampled once per round-trip when it hits the output coupler, and it is only the phase change modulo 2π that matters. Specifically,

$$\Delta\phi_{CEO} = \left(\frac{1}{v_g} - \frac{1}{v_p}\right) l_c \omega_c mod 2\pi \tag{2.15}$$

In the frequency domain this is a frequency offset meaning that the frequency is not at zero but starts precisely at ν_{CEO} while teeth are still ν_r distant from each other. In this way, the frequency of a generic n-th mode is

$$\nu_n = n f_{rep} + \nu_{CEO} \tag{2.16}$$

Both ν_{CEO} and f_{rep} are the two major parameters that, if controlled and stabilized, led to the Optical Frequency Comb.

The repetition rate (mode spacing) f_{rep} can be measured with a fast photodiode and compared or phase-locked to a microwave reference ν_{ref}. Alternatively, mode N of the comb can be heterodyned with a narrow emission linewidth external cw laser at frequency ν_{opt}. Active feedback to the frequency comb can force the comb mode to oscillate in phase with the cw laser, and as the other modes are already locked in phase via the mode-locking mechanism, f_r assumes the value of $f_r = (\nu_{opt} + \nu_{CEO})/N$.

In nearly all cases, ν_{CEO} is measured by frequency-doubling a portion of the octave-spanning spectrum obtaining $2\nu_n = 2(n f_{rep} + \nu_{CEO})$, and heterodyning it

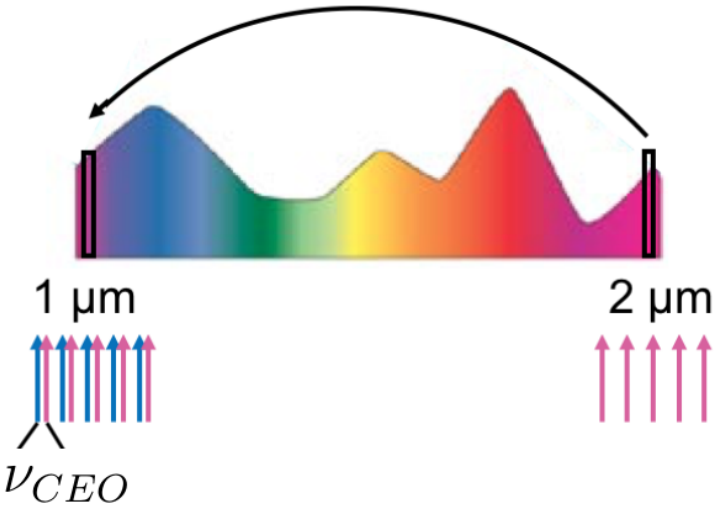

Figure 2.8: CEO frequency detection principle. The longer wavelength part (pink) of the spectrum is doubled and combined with original lower part (blue) to obtain the ν_{CEO}

with the existing comb elements $\nu_{2n} = 2nf_{rep} + \nu_{CEO}$. Their frequency difference is only the ν_{CEO} term. Measuring ν_{CEO} with narrower spectra is also possible, but with the requirement of a higher-order nonlinearity, e.g., third harmonic versus second harmonic.

2.3.2 Comb assisted spectroscopy: absolute frequency determination

With the introduction of the optical frequency comb synthesizer the measurement of an unknown optical frequency can be directly performed by means of the heterodyne method The frequency comb, fully stabilized so that each tooth frequency is well known by the relation 2.16, and the unknown laser frequency are combined into a fast photodetector. The photogenerated current at the output of the detector, as in the classical heterodyne method, presents components at frequencies

$$f_b = |\nu_L - \nu_{comb}| = |\nu_L - nf_{rep} - \nu_{CEO}| \tag{2.17}$$

By writing $n = N_L + l$ with N_L the number of the closest teeth to the laser frequency and l an integer number we can express 2.17 as

$$f_b = |\nu_L - N_L f_{rep} - \nu_{CEO} \pm l f_{rep}| = |f_{b_0} \pm l f_{rep}| \tag{2.18}$$

A periodic train of beat-note signals are present in the output spectrum of the photodetector. By filtering the photocurrent, the f_{b_0} beat-note can be easly measured by an electronic frequency counter (Fig.2.9). The determination of the integer order N_L can be obtained using a wavemeter (WM) in order to measure

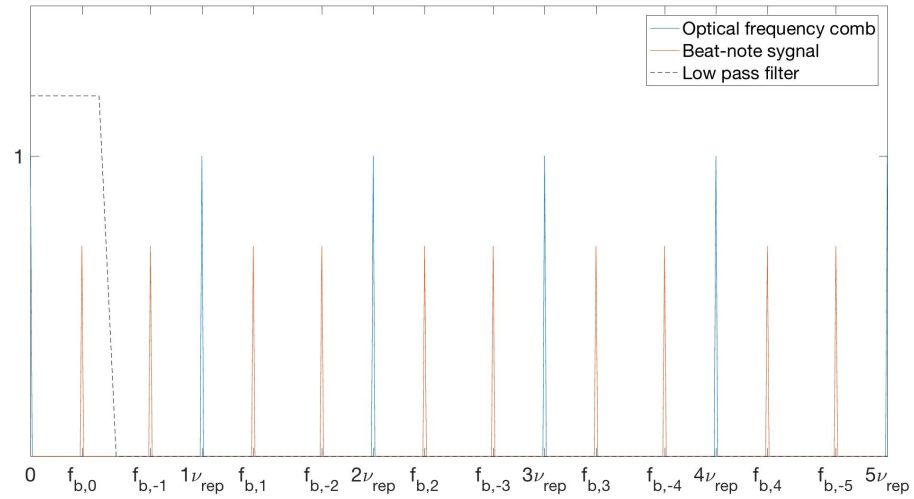

Figure 2.9: Representation of frequency spectrum of heterodyne detection between an optical frequency comb and an unknown CW laser. Blue lines comb spectrum. Orange line train of beat-note signal. Black dashed line represent a low pass filter

ν_L with an accuracy better than $f_{rep}/2$

$$N_L = \frac{\nu_{WM}}{f_{rep}} \tag{2.19}$$

Alternatively, N_L can be determined by changing the comb repetition frequency by a small amount $f_{rep} + \delta f_{rep}$ and measuring the beat-note deviation Δf_b, so that

$$N_L = \frac{\Delta f_b}{\delta f_{rep}} \tag{2.20}$$

Once the N_L integer is determined, the unknown CW frequency is then:

$$\nu_L = N_L \nu_{rep} \pm f_{beat} + f_{CEO} \tag{2.21}$$

2.4 Comb state of art

During the past decade, the increased interest in optical frequency combs has resulted in the development of new femtosecond laser sources, as well as the re-visiting of existing sources with a focus on the frequency domain properties. The rapid progress of frequency combs at the turn of the century benefited greatly from development in the 1990's of robust femtosecond solid state lasers, such as those based on Ti:sapphire the first ones to be spectrally broadened to an octave and self-referenced.[23] After that several other laser sources have been employed as optical frequency comb. In figure 2.11 is shown a graphical representation of some available optical frequency comb divided by spectral window.

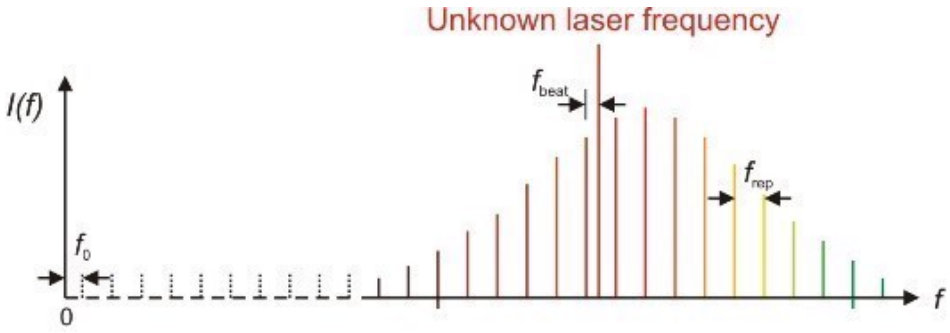

Figure 2.10: Absolute frequency emission determination with Optical Frequency Comb

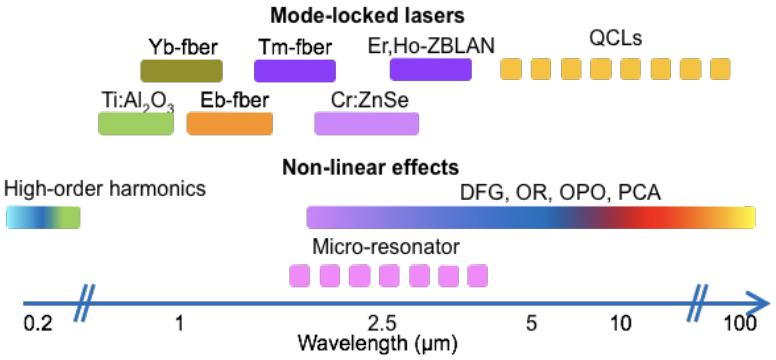

Figure 2.11: Optical frequency comb state of art. Graphical representation of available technology for each spectral window

Different technique can be exploited in order to generate an optical frequency comb. A first choice is to use a bulk solid state laser mode-locked such as Ti:sapphire covering the visible, rare-Earth (Ytterbium or Erbium) doped crystal and glasses emitting in near-infrared region [24][25] and very recently Chrome doped crystal such as Cr^{2+}:ZnSe or Cr^{2+}:ZnS operating near 2.5 μm [26][27][28]. However, such lasers are rarely used in real-life applications outside the research lab environment, owing to their complexity, very poor environmental stability, large size, large power consumption, and reliance on water cooling. More recently the emergence of fiber lasers, based on robust commercial optical fiber technology, have driven a rapid development of the fiber-laser frequency comb technology and thanks to small size, high efficiency, low price and remarkably optical properties, they will become the inevitable trend in the technological development of optical frequency combs[3][29]. Erbium-doped fiber operating near 1.5 μm has profound influence on the optical fiber communication technology [30] [31]; Ytterbium-doped fiber offers higher efficiency as well as larger gain bandwidth [32][33][34][35]; Thulium- and Holmium-doped, operating around 2 μm wavelength, are also very important for many applications in nonlinear optics, medicine and sensing [36][37][38][39][40].

Very few demonstration of fiber laser sources at wavelengths beyond 3 μm have

been obtained. By contrast quantum cascade lasers can be tailored to operate at nearly arbitrary wavelengths in mid and far infrared spectral region operating also in mode-locking regime [41][42][43]. However, the comb properties of these rather narrow (<50 cm^{-1}) emission spectra have not yet been tested. In most cases, a different route is taken to access the spectral region beyond 3 μm, in which nonlinear optical effects are harnessed to transfer electromagnetic energy from the visible or near-infrared domain into the mid-infrared[44]. For example, all modes of a near-infrared frequency comb can simultaneously be subjected to difference-frequency generation (DFG) [45]. When mixed with a continuous-wave (CW), the modes of a comb can correspondingly be transferred in the mid-infrared domain for an appropriately choose of CW frequency. The efficiency of this process depends on the strength of the optical nonlinearity and also on the ability to achieve phase-matching over the wide necessary bandwidth [46]. DFG between two synchronized combs is also possible, at cost of more complexity [47]. Alternatively, difference-frequencies can be generated between the different teeth of a single comb. In this case the combs carrierenvelope offset frequency is fixed to zero, which simplifies the control of the comb structure [48][49][50].

A key challenge in sources based on nonlinear optics is the efficiency of the desired photon-conversion process. One way of boosting efficiency is to use an optical parametric oscillator (OPO). If pumped by a femtosecond laser, many longitudinal signal modes of the resonator in an OPO can simultaneously experience gain that exceeds the threshold for parametric oscillation. Of course, achieving oscillation for the many signal and idler modes requires, in addition to phase matching, management of the resonators dispersion to ensure that the equidistant signal modes coincide with the resonators modes across the desired wide bandwidth[51][52][53].

Recently, researchers have reported that a special form of parametric oscillation (sometimes referred to as hyper-parametric oscillation [54]) can be used to generate a frequency comb in an optical microresonator. The resonator comprises a toroidal ring of sub-millimeter diameter that can sustain very-high-quality optical whispering-gallery modes. If populated with a strong pump field, the third-order nonlinearity of the dielectric resonator material can lead to four-wave mixing. A single-frequency pump laser can give rise to a signal-idler pair, and also to a massive cascade of signal and idler sidebands that become mutually phase-locked by non-degenerate four-wave mixing. The resulting Kerr comb can cover an entire octave and extend into the mid-infrared if pumped by a strong near-infrared laser [55][56] [57].

An intense effort has been spent in the past few years to extend frequency combs toward also the UV regions where electronic transitions of single atoms, molecules, and ions can be used for metrological purposes, as a test for variation of fundamental constants, or for the development of novel primary temporal [58]. Frequency doubling and quadrupoling of Ti:sapphire lasers, either outside or within enhancement cavities, is used to achieve milliwatt-level combs in the UV range [59]. Scaling toward the XUV range is far from trivial, since high-harmonic generation (HHG) processes in gas jets need to be exploited in the high-repetition-

rate regime [60].

Chapter 3

Comb-assisted Doppler-free spectroscopy of CHF_3

In this experiment a Quantum Cascade Laser (QCL) is coupled in a 30 cm cell filled with few Pascal of CHF_3 in a double pass configuration in order to measure saturated absorption profiles. Absolute frequency measurement is performed by phase locking the QCL to a mid-infrared optical frequency comb synthesizer. Changing the repetition frequency of the comb, keeping the QCL phase-locked to the comb itself, it is possible to scan the frequency of the QCL around the absorption spectra of the molecule. The major aim of this experiment is to fully characterize CHF_3 absorption spectra in 8.6 μm region. In particular we focus on the saturated absorption line profile to precisely address absorption line center frequencies, line broadening coefficients and saturation intensities

3.1 Experimental setup

Figure 3.1 shows the experimental setup for Doppler-free comb assisted spectroscopy of the CHF_3 molecule. A Quantum Cascade Laser (QCL) with a tunable frequency from 1155 cm^{-1} to 1160 cm^{-1}, with a maximum optical power up to 50 mW and a linewidth of 1MHz is used as probe beam. After emerging from a 30-dB optical isolator, the QCL output beam is collimated by a ZnSe plano-convex lens (200mm focal length) followed by a 50/50 beam splitter (BS1) whose reflection propagates as the strong pump beam through a 25 cm long stainless-steel cell (equipped with anti-reflection coated ZnSe windows) containing the CHF_3 gas sample (98% purity) at room temperature, T_{room}, with a measured beam waist diameter of 2.1 mm in the middle of the absorption cell as measured with a CCD camera.

Reflection from a second 50/50 beam splitter (BS2) is directed to a liquid-nitrogen-cooled HgCdTe (MCT) detector (1-MHz electrical bandwidth), PD_{lin}, to record the single-pass absorption; reflection from BS2 passes through a 50mm focusing lens and it is back-reflected by a mirror to generate the counter-propagating weak probe beam (1/4 of the pump beam power) which is then superimposed to

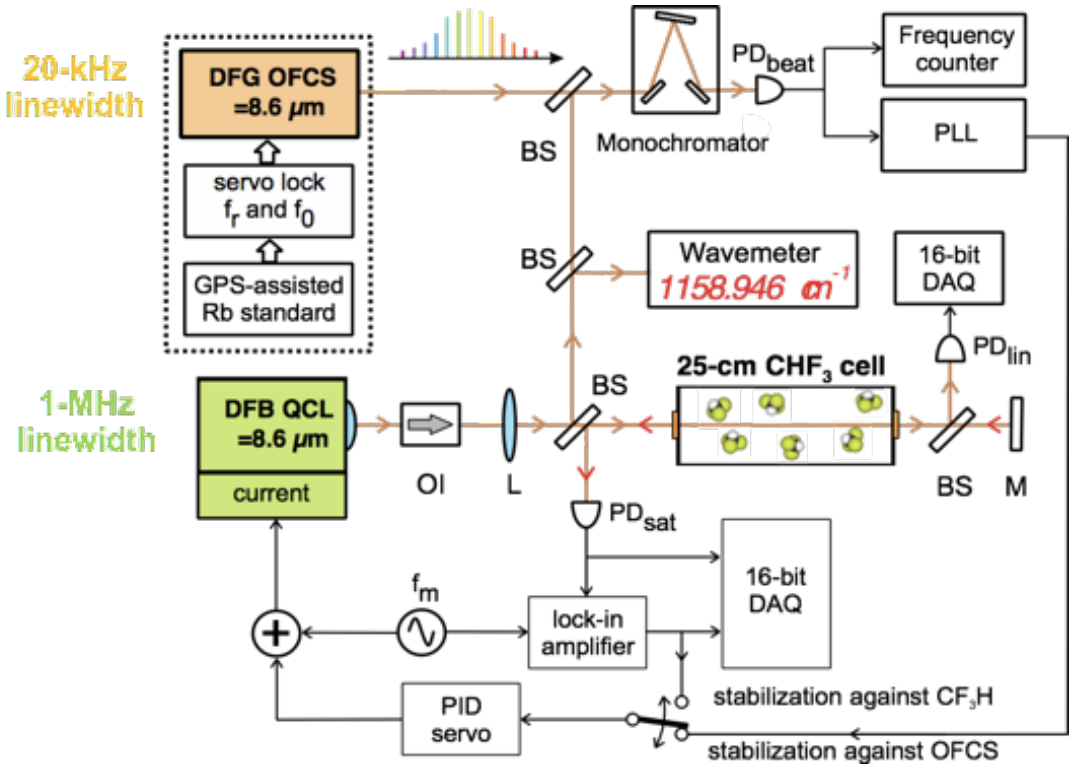

Figure 3.1: Experimental setup for Doppler-free FM spectroscopy of CHF_3 at 8.6 μm. BS: beam splitter; DBM: doubled-balanced mixer; DFG OFCS: difference-frequency-generation optical frequency comb synthesizer; L: lens; M: mirror; OI: optical isolator; PID: proportional-integrative-derivative servo.

the pump beam in the gas cell with matched phase fronts (probe beam waist diameter of 1.8 mm). To detect the saturated absorption signal, the probe beam is transmitted by BS1 onto a four-stage thermo-electrically cooled MCT detector (50 MHz bandwidth), PD_{sat}.

The first transmission of BS1 is superimposed to a Difference Frequency Generation Optical Frequency Comb (DFG-OFC) at 8.6 μm whose repetition frequency is stabilized against a radio-frequency (RF) synthesizer locked, in turn, to a GPS-disciplined Rb clock. This Rb standard has a fractional stability (1-s Allan deviation) and accuracy of $8 \cdot 10^{12}$ and 10^13 respectively. After filtering by means of a 0.01 μm monochromator, the combined beams are focused onto a 200-MHz bandwidth MCT detector, PD_{beat}, ($5.7 \cdot 10^4$ V/W responsivity and 50 nV/pHz noise floor at a temperature of 77 K).

This beat note is stabilized at 70 MHz against a frequency synthesizer through a phase-detector using a proportional-integrative-derivative (PID) servo controller acting on the QCL driving current.

3.2 Quantum Cascade Laser

The development of QCL [61] allows a new and easier access to mid-infrared (3-15μm) region with a modest/high power, narrow line and tunable single frequency laser source. The emission central wavelength of 8.6 μm was chosen in accordance to an important transition of the tri-fluoromethane (CHF_3) gas molecule where the line center is strongly influenced by the proton to electron mass ratio [11]. A commercial single spatial mode and single longitudinal mode Distributed Feedback Quantum Cascade Laser (DFB-QCL or QCL) The DFB-QCL operates at room temperature (few mK of thermal stability provided by the thermal control) with a maximum output power of 50 mW at 8.6 μm and slightly astigmatic beam with a quality factor $M^2 = 1.1$. A low-noise commercial current driver (Wave-length Electronics QCL1500), with a nominal current noise spectral-density of 3 nA$\sqrt{Hz}$ and a 2 MHz modulation bandwidth, has been employed.

This source is tunable in power and wavelength by changing both injected current and working temperature..

The frequency noise power spectral density of the QCL and its emission linewidth was measured with an optical frequency discriminator based on the sideof CHF_3 absorption line. This noise refers to random fluctuations of instantaneous frequency of an oscillating signal. The instantaneous frequency is defined as

$$\nu(t) = \frac{1}{2\pi}\frac{d\phi}{dt} \tag{3.1}$$

and it is essentially the temporal derivative of the oscillation phase ϕ. Any deviation from a linear phase is considered noise. In the experiment, the frequency noise is retrieved from a measurement of the intensity fluctuation of the laser after interaction with an amplitude to frequency converter. The adopted discriminator was a side of an absorption line of CHF_3. The measured spectrum of the transmitted intensity reproduces the spectrum of the laser scaled by the slope of the absorption profile at around the operating point (Fig.3.2). If $S_{\Delta\nu}(f)$ is the power spectral density of frequency noise [Hz^2/Hz] it can be converted in power spectral density of amplitude $S_I(f)$ [V^2/Hz] by a slope discriminator as

$$S_{\Delta\nu}(f) = \frac{S_I(f)}{D^2} \tag{3.2}$$

Figure 3.3 shows the measured power spectral densities of the QCL with RIN contribution.

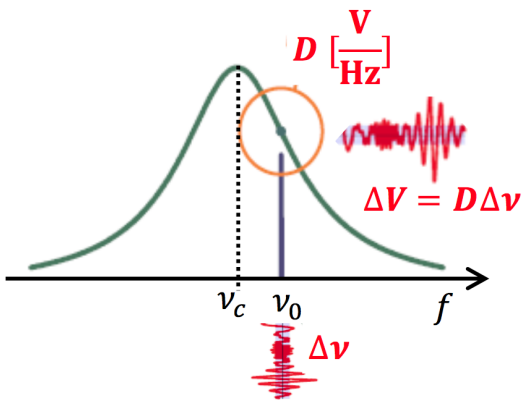

Figure 3.2: Frequency to amplitude conversion provided by an absorption line

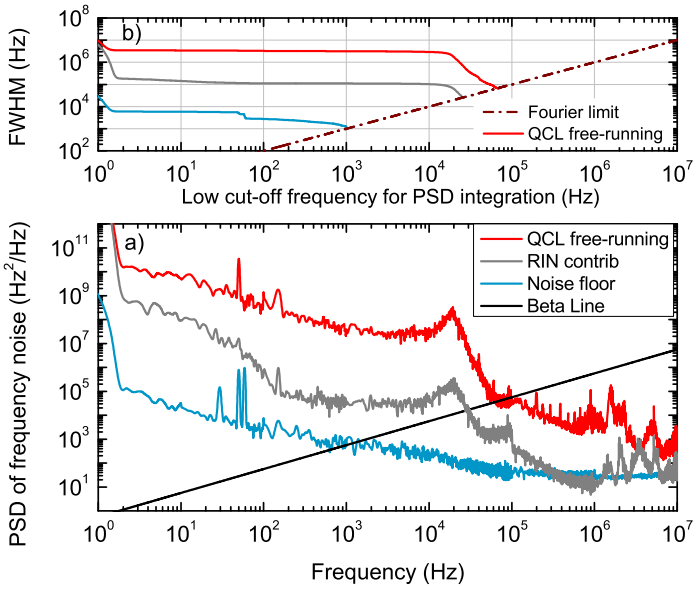

Figure 3.3: Bottom figure :Frequency noise PSD of the QCL laser i(dark-gray line) together with the RIN contribution (blue), the noise floor (gray), and the β-line, $8 \ln 2 \pi 2 f$ (black). Top figure: calculated emission linewidth versus integration bandwidth. Inset: beat signal (green line) between the DFG-comb and a narrow-linewidth laser at 8.6 μm, together with its Gaussian fit (black line).

3.3 Optical Frequency Comb

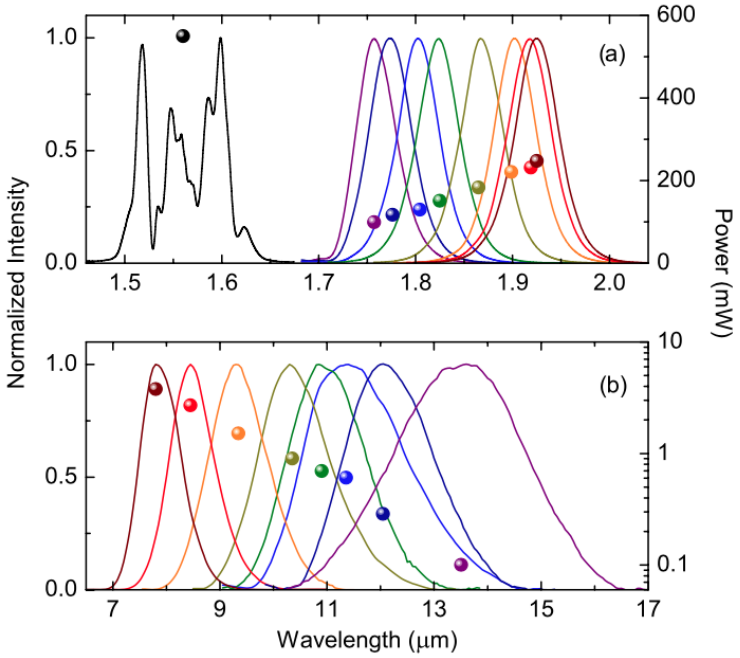

Figure 3.4: (Color online) Spectra (left axis) and average power (dots, right axis) of pump and signal pulses (a) and of the generated mid-IR pulses (b).

The self-referenced optical frequency comb at around 8.6 μm is synthesized by a different frequency generation process. The laser source chosen is a MenloSystems M-Comb Erbium doped fiber laser with a repetition rate f_r of 250 MHz. This frequency is choose to be high enough to have teeth well separated in the spectral domain, important point for spectroscopy, and not so high to lose peak power P_{peak} on the pulse, given by $P_{peak} = P_{avg}/f_r t$, with t pulse duration. The comb repetition rate f_{rep} was locked to an RF synthesizer referenced to a GPS-disciplined Rb frequency standard .

The commercial source is equipped with two indipendent amplifier stages each providing 0.5W averege power, femtosecond pulse train at 1.55 μm already provided with a self-frequency-shifted Raman soliton covering from 1.76μm to 1.93μm with an average power of 200 mW spread over the whole spectrum. This process is created starting from one of the 1.55 μm output and exploiting the Raman shift effect [62] of nonlinear fibers [63].

In order to reach mid-IR region, the second 1.55 μm output, pump, and the Raman shifted soliton, signal, are superimposed on a non-linear crystal, GaSe, which combines high non-linearity with good transparency at this wavelength and high damaging threshold. It is possible to tune the idler output frequency by changing the Raman soliton wavelength with a corresponding adjustment of the temporal overlap and phase-matching angle. The generated mid-IR spectra recorded with a grating monochromator are shown in Fig. 3.4 together with the

corresponding average output power levels. Mid-IR radiation spans from $8\mu m$ to $14\mu m$ with an increasing spectral width from 0.8 to 3 m when moving toward longer wave- lengths, as a result of the improved group velocity matching between signal and idler pulses in GaSe. The mid-IR output power peaks at 7.8 m with 4 mW (0.22 W per comb tooth), it remains in excess of 1 mW up to 10.2 m (55 nW per comb tooth) while decreasing down to 110 W (6 nW per comb tooth) at the maximum DFG wavelength of 13.6 m. This power drop is due to the combination of reduced optical power in the SFS soliton, onset of linear absorption in GaSe for wavelengths above 12 m and a strong decrease of the diffraction length of the idler pulse for wavelengths comparable to the spot size dimension. [64] Among the different approaches pursued so far to generate optical frequency combs in the mid-IR spectral region, the DFG process is very appealing because it provides intrinsic stabilization of the comb, due to the passive cancellation of the offset frequency (ν_{CEO}) as well as the suppression of common mode noises of pump and signal arms. The result is a narrow-linewidth harmonic comb, with the pulse repetition frequency (f_{rep}) as the only free parameter. This removes the need of further stages in order to detect and lock ν_{CEO}.

The comb ν_{rep} was locked to an RF synthesizer referenced to a GPS-disciplined Rb frequency standard.

3.4 QCL-OFC lock

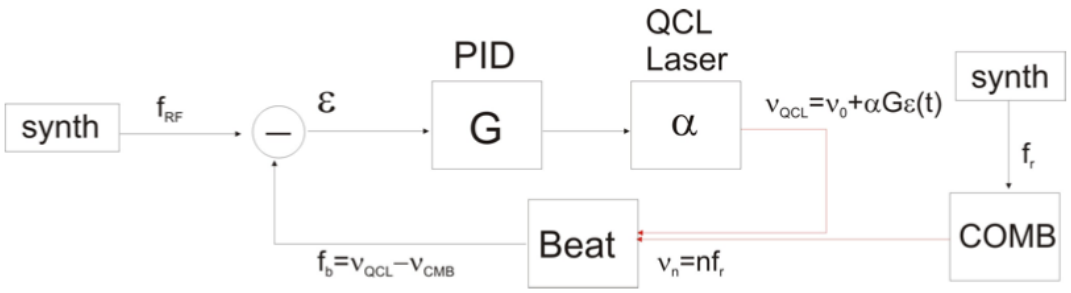

Figure 3.5: General scheme for locking between QCL and OFC with a PID controller

The free running QCL has a 1-MHz linewidth in a 1 ms integration time while the DFG comb modes characterized with a narrower linewidth of 20kHz. Comb linewidth wes measured by heterodyne detection with an another QCL with a 4kHz linewidth Fig. 3.7(inserto). In this experiment mid-IR tooth has been used as a transfer oscillator to phase lock the QCL in order to, at the same time, shrink its linewidth and having an absolute reference for frequency measurement.

Fig. 3.5 shows the schematic for the implemented phase-locking-loop. A beat note between QCL and OFC is created by superimposing them on a beam splitter and, passing through a monochromator, it is measured by a 200-MHz bandwidth

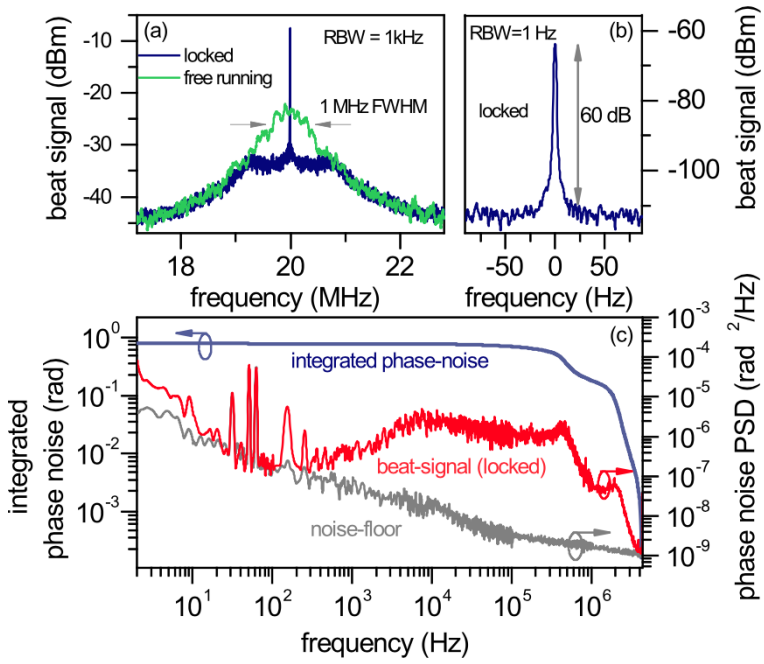

Figure 3.6: A beat-note signal between the mid-IR comb and the QCL free-running (green curve) and the phase-locked (blue curve) QCL. (b) Phase-locked beat note with higher resolution. (c) Phase noise PSD and integrated phase noise versus integra- tion bandwidth.

MCT detector, PD_{beat}, (5.7104 V/W responsivity and 50 nV/pHz noise floor at a temperature of 77 K). The measured signal passes through a 50dB amplifier, a 70 MHz band pass filter (10 MHz bandwidth). In order to achieve a tight phase locking the beat-note phase noise has to fit inside the 2π detection range of the phase detector. In this sense the beat-note was initially shifted in frequency with a local oscillator set at 890 MHz, divided by 16 obtaining a final beat-note centered at 60 MHz and then compared with a local oscillator in a phase and frequency detector. The error signal is further processed by a PID controller and then fed back to the current driver of the QCL diode. Fig.3.6(a) shows the comparison between unlocked beat-note with a 1 MHz line-width in a 1 kHz resolution bandwidth and the phase locked condition with an impressive 30 dB contrast which increases up to 60 dB in a 1 Hz RBW, as shown in fig.3.6(b). A 500 kHz phase-lock control-bandwidth can be inferred from the spectral-shape of the closed-loop beat note signal. The phase-lock performance was characterized, in terms of residual phase noise, by measuring the power spectral density (PSD) of the error signal at the output of the phase detector. Fig.3.6(c) shows the measured phase-noise PSD (right axis) together with the integrated residual phase noise (left axis).

We characterized the frequency-noise properties of the QCL by using the side of a Doppler broadened CHF_3 line as an optical frequency discriminator and by measuring the frequency-to-intensity converted noise-PSD. In tight-locking con-

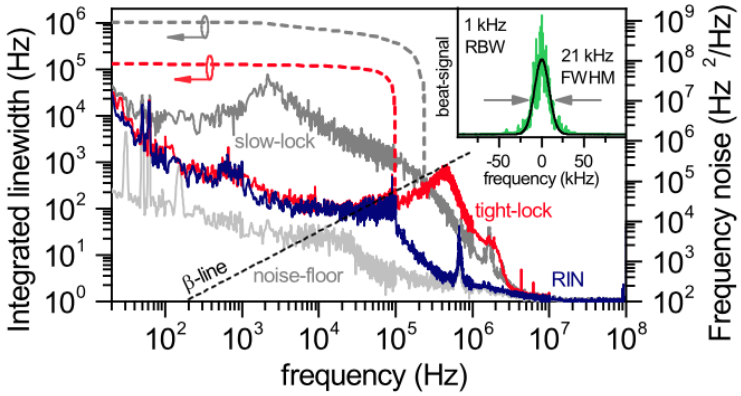

Figure 3.7: Right axis: frequency noise PSD of the QCL laser in slow-lock (dark-gray line) and in phase-locked (red line) conditions together with the RIN contribution (blue), the noise floor (gray), and the β-line, $8 \ln 2 \pi 2 f$ (black). Left axis: calculated emission linewidth versus integration bandwidth. Inset: beat signal (green line) between the DFG-comb and a narrow-linewidth laser at 8.6 μm, together with its Gaussian fit (black line).

ditions, the integrated value of ∼130 kHz (red dashed line of Fig. 3.7), entirely due to the RIN contribution, fixes an upper limit for the QCL linewidth.

After locking, we can finely tune the QCL frequency only by acting on OFC repetition rate, so that a δf_{rep} is transfered as $\delta f_{QCL} = n * \delta f_{rep}$ where n is the tooth order.

3.5 Direct saturated spectroscopy of CHF_3

In these first measurements we investigate on linewidth and shift of absorption transition due to pressure effect. These measurements are performed, as already said in previous chapter, by locking the OFC repetition frequency to a synthesizer referenced to the Rb clock and by locking of the QCL to the OFC stabilizing their beat note. Thanks to this, QCL can be scan across the line profile only by changing the repetition rate, always maintaining an absolute frequency calibration. Signal coming from PDsat is acquired by a 16bit 40kSa ADC with an integration time of 0.5s. Qcl power at gas cell is set to 5 mW.

A first characterization of the absorption lines around $1158,907 cm^{-1}$ was performed applying a current ramp to the QCL. Signal coming from PD_{sat} was recorded with an oscilloscope triggered with the ramp. In addiction a first wavelength modulation technique was execute by applying a modulation on the current ramp.

Both the measurement are reported in fig.3.8. (X-axes is time).

For this work we focus on two different lines: "Riga1" ${}^rR_{36}(38)$ and "Riga2" ${}^rR_{39}(44)$.

First data have been the registration of the entire absorption lines.

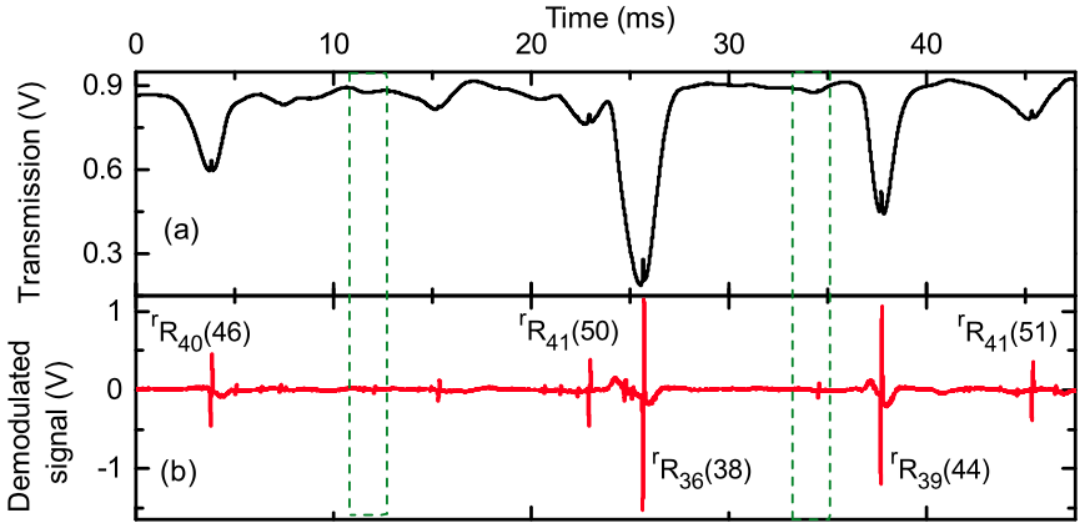

Figure 3.8: Saturated absorption (a)and FM dispersive (b)signal from a 25-cm-long cell filled with CHF_3 gas sample at 10 Pa.

In Figure 3.9.a) we can see the baseline, without gas, and an absorption line at 8 Pa of Riga2. We can notice that baseline is not flat. This is due to optical feedback, any reflection of the QCL beam from optical element that are back reflected to the source, create an interference patter. This effect is reduced thanks to the optical isolator but it is not completely suppressed, so for every scan we need to measure baseline and subtract from absorption line profile.The double pass measure clearly show a Lamb dip created by saturation effect. Several measurement has been taken with different pressure for the two lines. (In fig 3.9.b) example scanning of Riga2)

A simple fitting with a Gaussian function for the Doppler line and a Lorentzian function for the Lamb dip has been implemented to retrieve line-center, linewidth and line-intensity. This model is not accurate because as illustrated in first chapter a single line profile should be Voigt and , beside that, what we call absorption line in reality is a convolution of more than one transition.

Before fitting all the measurement coming from PD_{Sat} were normalized respect to the empty cell baseline. Fig. 3.12 shows measured absorption profile ($\alpha = -\ln(T/T_0)$ with T transmitted signal and T_0 baseline) and their fitting curve for different pressure. Despite normalization, fringes are still present and non-negligible for the lower pressure. Interference fringes are not a fix patter and, from a measure to another, they change. First of all this is due to the change of the refractive index of the cell that change with the gas pressure. Beside that, also for the same pressure measure registered in different time present different pattern. Because of this we can not completely cancel out this kind of parasitic effect. However, line profiles seems to be right fitted by our model except for lower pressure where interference fringes became comparable with the signal an so they create a distortion of the profile. Looking in the residual of the fitting process we can see a structured pattern, periodic, that can again be linked to these fringes.

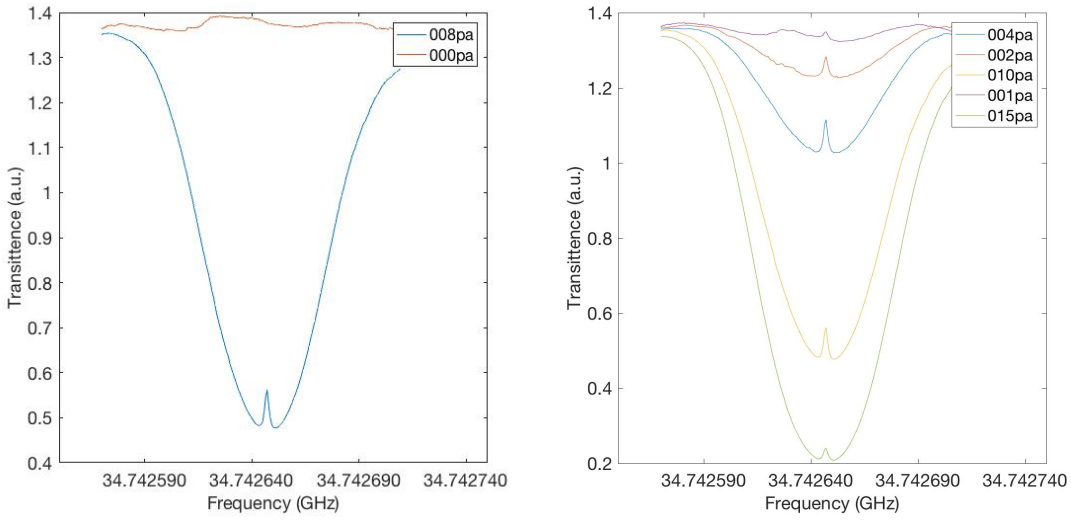

(a) *(b)*

Figure 3.9: a) Riga2 line profile at 6 Pa with a baseline (empty cell). b) Riga2 line profile for different pressure: 1 Pa, 2 Pa, 4 Pa, 10 Pa, 15 Pa

Quantitative data coming out from this data analysis are not all reliable, particularly for what concern Lamb dip due to a too low number of point in the dip sample. I need to underline that our cell suffer for leakage. This fact limit the total measurement time, up to 150s, in order to limit the pressure variation to 10% of its initial value. This is reflected on the maximum number of point per scan, up to 200 point, since for every point we need to spend about 0.8s (due to communication, stabilization and integration time of the measure).

To better understand and characterize the Lamb dip we focus our scan only in the neighbor of this. Fig. 3.13 and fig. 3.14 show an example of this short scan. Fitting looks very good at least for pressure higher than 2 Pa, still because of fringes but also for a lower signal to noise ratio.

Fig.3.10 reports the full width half maximum of the fitted data as a function of pressure .

The full width at half maximum of this two lines are in the same range from 2 to 3 MHz and they follow the same trend. The FWHM decreases with the decreasing pressure down to a minimum over which it restart to grow. This can be addressed to the combination between power and pressure broadening. Pressure broadening is reducing while power broadening is increasing at low pressure.

Moreover, line center frequency is difficult to interpret. We expect a pressure shift but uncertainty of result can not allow to identify a clear trend. An improved fitting model should be provided in order to clearly identify both these effects.

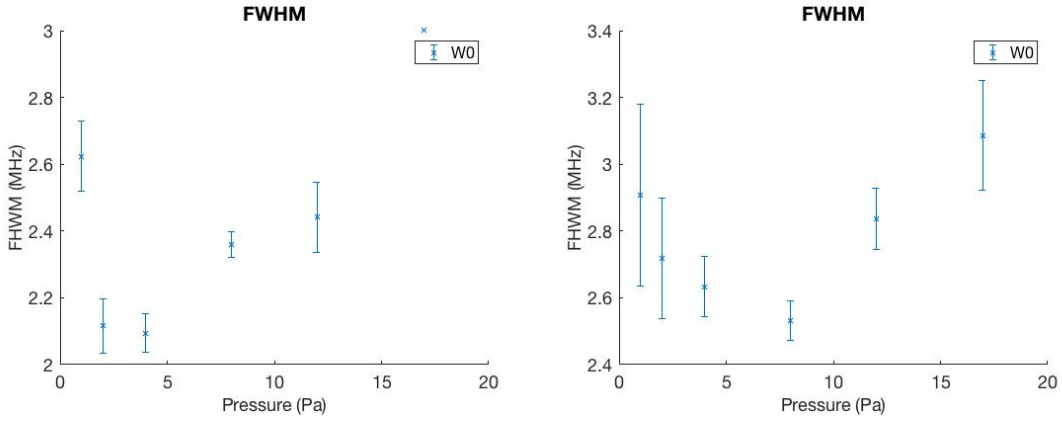

(a) Riga1 *(b) Riga2*

Figure 3.10: Fitted full width at half maximum as function of pressure for a) Riga1 and b) Riga2. Error bar correspond to 95% confidence intervals of fitting.

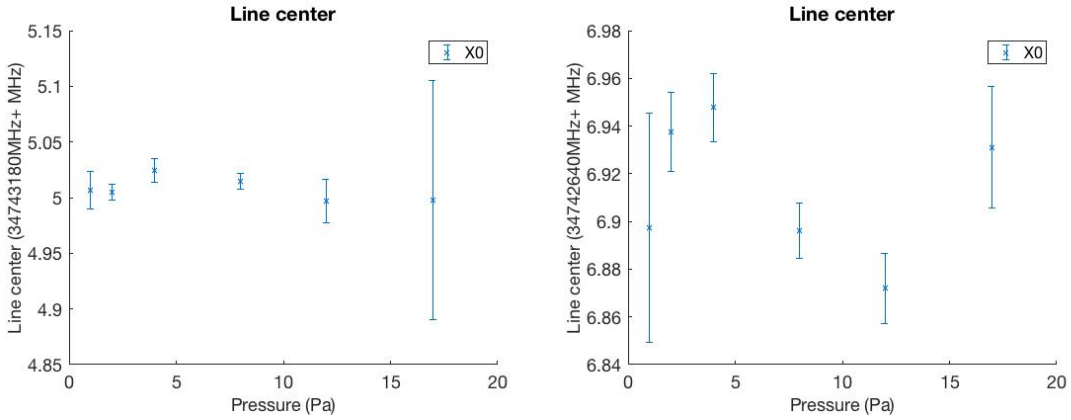

(a) Riga1 *(b) Riga2*

Figure 3.11: Fitted line center as function of pressure for a) Riga1 and b) Riga2. Error bar correspond to 95% confidence intervals of fitting.

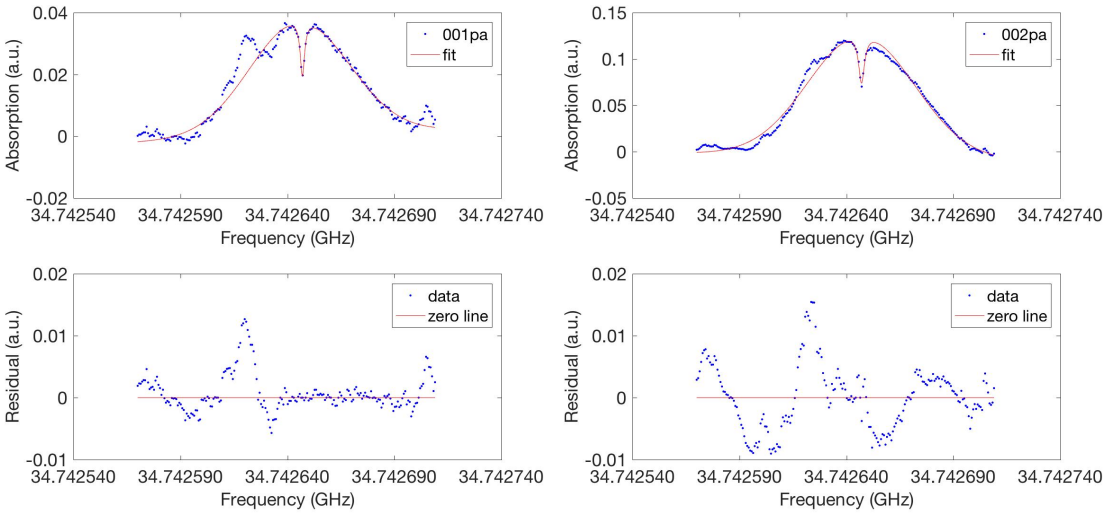

Figure 3.12: Riga2 absorption profile, fitted curve and residual plot for 1pa, 2pa, 4pa e 10pa

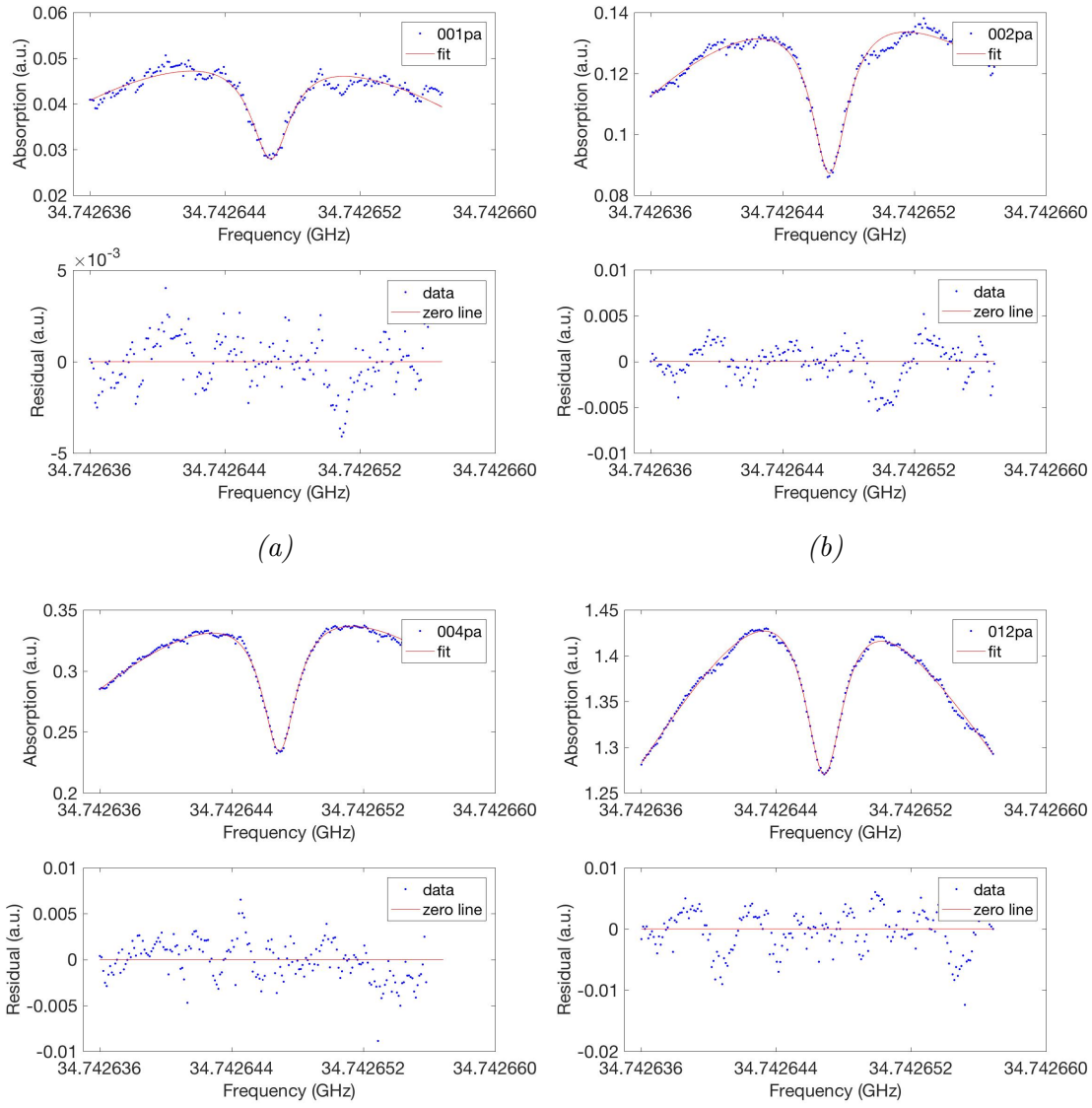

Figure 3.13: Riga2 absorption profile in dip proximity, fitted curve and residual plot for 1pa, 2Pa, 4Pa e 10Pa in the Lamb dip proximity

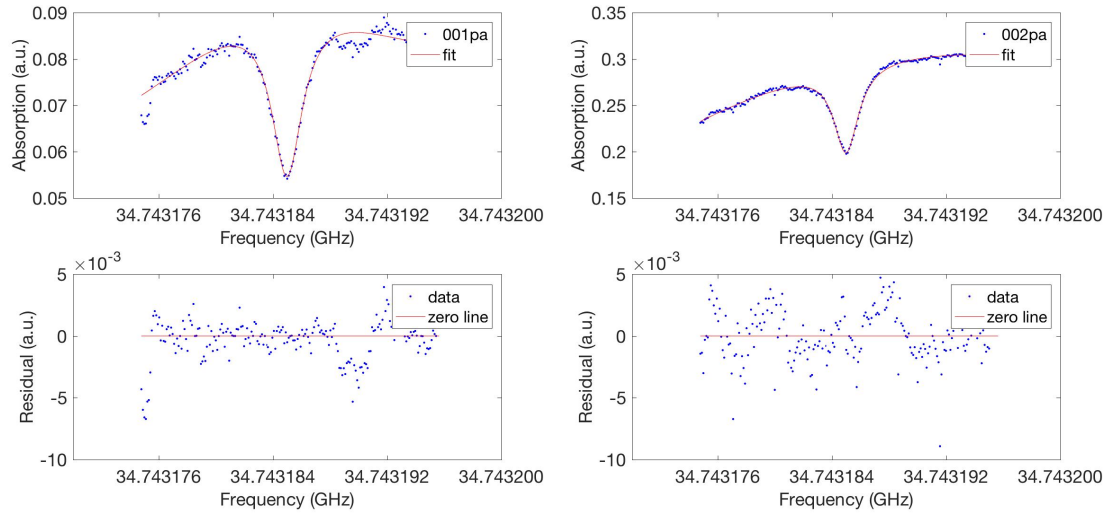

Figure 3.14: Riga1 absorption profile in the dip proximity, fitted curve and residual plot for 1Pa, 2Pa, 4Pa e 8Pa

3.6 Wavelength modulation saturation spectroscopy of CHF_3

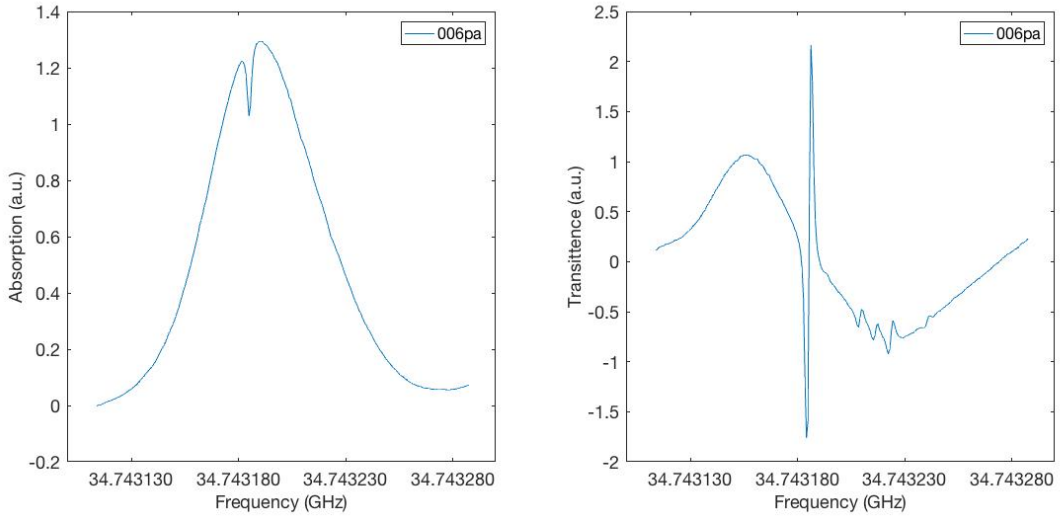

(a) *(b)*

Figure 3.15: Comparison between absorption profile of Riga1 recorded in direct a) and wavelength modulation b) setup at 6Pa

In order to improve our setup performance we implement a wavelength modulation technique. We introduce a wavelength modulation around 10 kHz with an amplitude of 320 kHz on the reference signal that we use to stabilize the beat note between QCL and COMB. Thanks to the locking also the beat-note signal is modulated and as consequence the QCL frequency. This kind of measurement has two main advantage: first it increases the signal to noise ratio and, as second, it has in output the derivative of the signal decreasing significantly the effects of parasite etalon fringes.

Fig. 3.15 shows the same absorption line for the same nominal pressure of 6 Pa with the direct method and the wavelength modulation. With this new method now we can easily distinguish more that one saturated absorption profile within the same Doppler broadened profile.

With this new setup we repeated the same measurement for the entire line and the dip zoom(Fig. 3.16). Still looking for quantitative result, Lamb dip has been fitted. In this case the fit is base on the derivative of a Lorentzian function added on a linear base signal. Fitting looks good; from residual it is evident that fringes effect are now canceled out, or not observable, but a "W" structure is now evident.

An improved model included high order derivative of Lorentzian properly weighted has been tried but no significant benefit has been highlighted. This could be addressed to the Lorentzian profile itself that is a good approximation

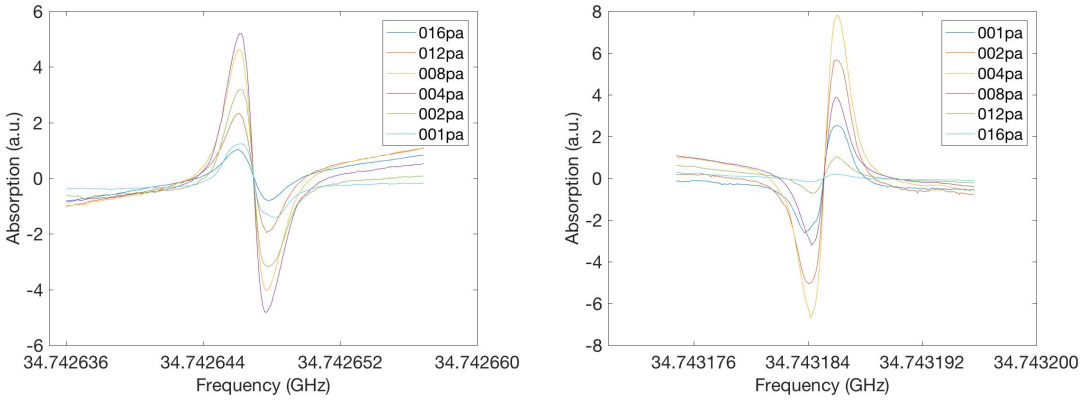

(a) Riga2 *(b) Riga1*

Figure 3.16: Dispersion curves of Riga2 a) and Riga1 b) for different pressure

but not a real description. This is evident looking to low pressure measurement. Fitted curve for 1 Pa e 2 Pa is now very far from their experimental data. This can be due to the fact that at higher pressure the main cause of broadening is the self collisions (with Lorentzian distribution), instead for low pressure transit time is the limiting factor (with Gaussian distribution).

Another possibility can be the effect of lock-in integration time with respect to the acquisition time between two consecutive data points. Further modeling have to be develop to clearly understand these effects.

Aware of this, FWHM and line center of the Lamb dip are plotted in fig. 3.17 and fig. 3.18.

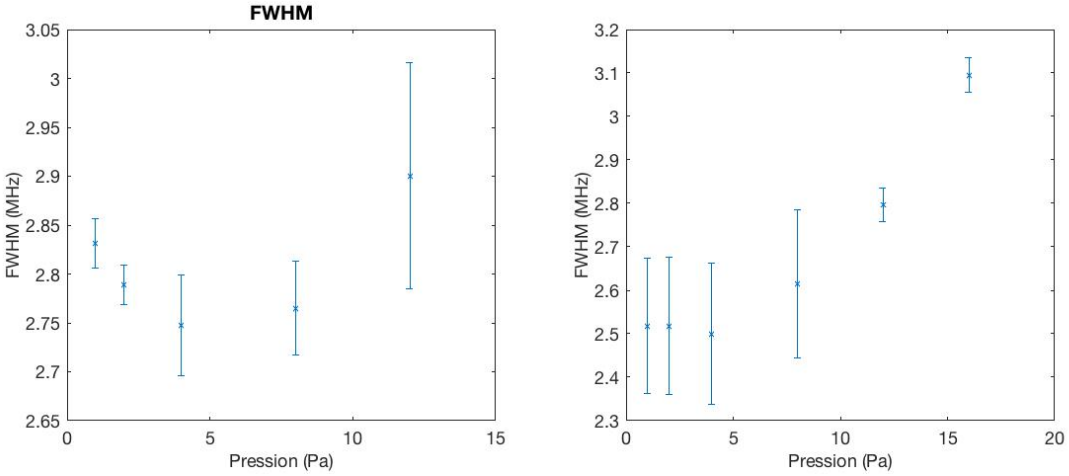

(a) Riga1 *(b) Riga2*

Figure 3.17: Fitted full width at half maximum as function of pressure for a) Riga1 and b) Riga2. Error bar correspond to 95% confidence intervals of fitting.

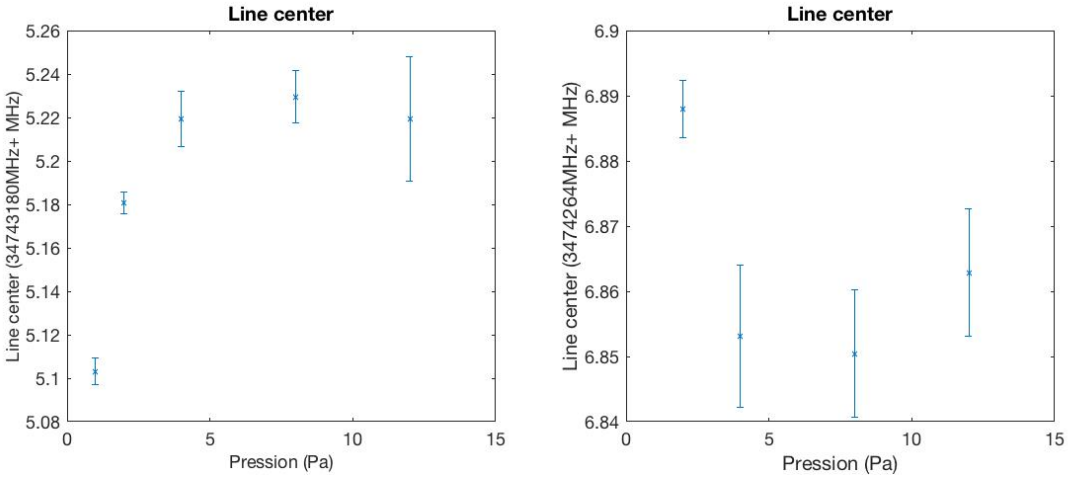

(a) Riga1 *(b) Riga2*

Figure 3.18: Fitted Dip line center as function of pressure for a) Riga1 and b) Riga2. Error bar correspond to 95% confidence intervals of fitting.

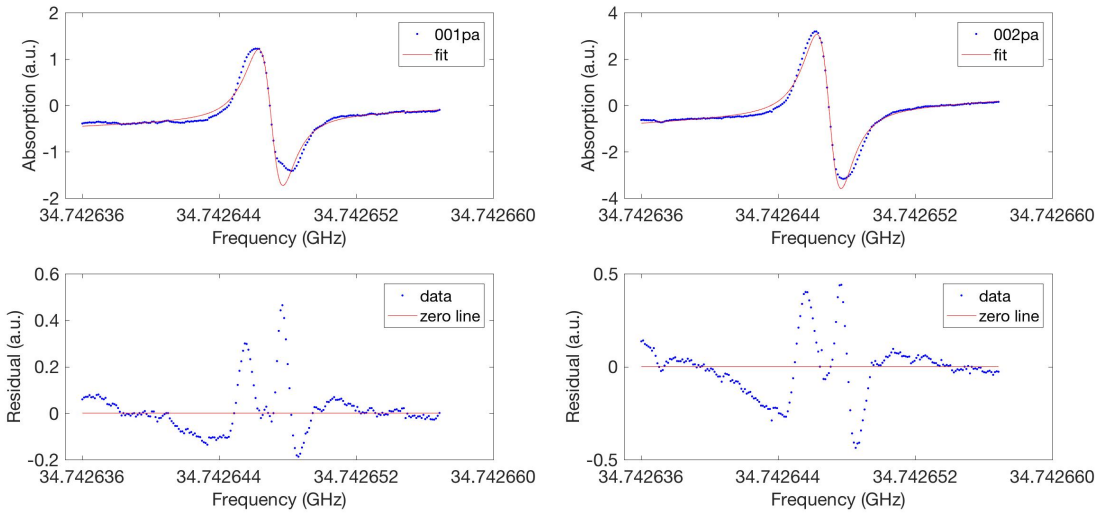

(a)

(b)

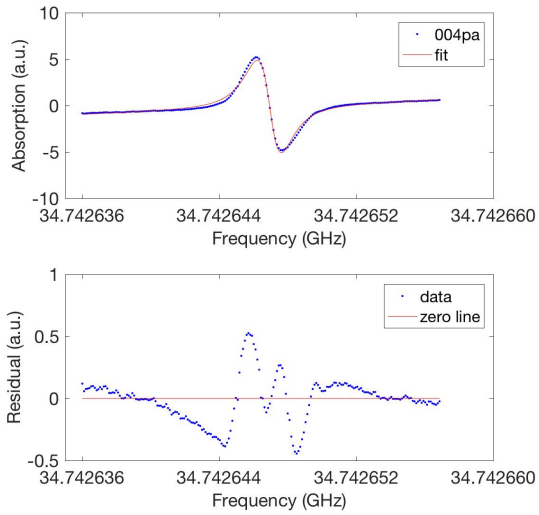

(c)

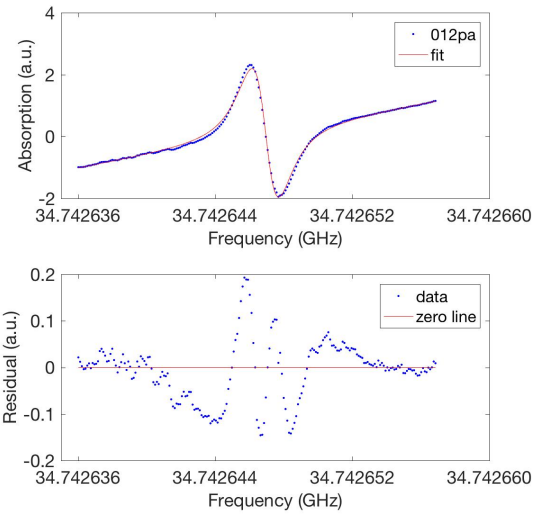

(d)

Figure 3.19: Riga2 absorption dispersion, fitted curve and residual plot for 1pa, 2pa, 4pa e 12pa in the Lamb dip proximity with wavelength modulation technique

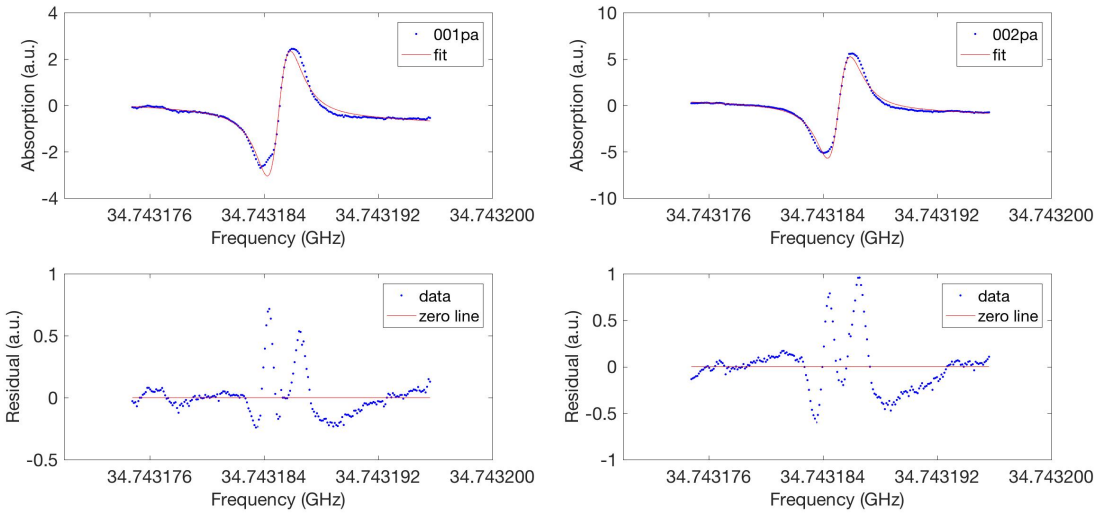

(a)

(b)

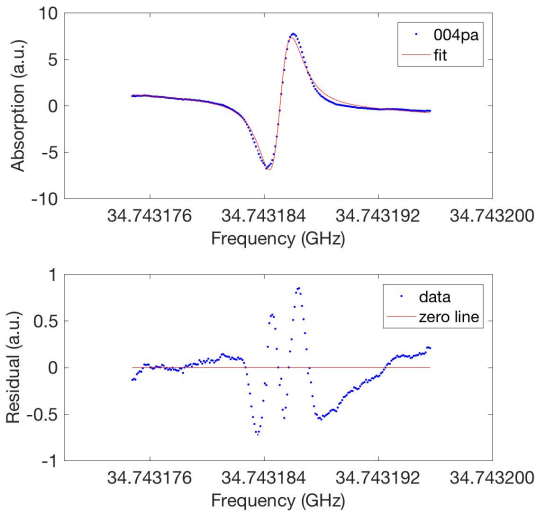

(c)

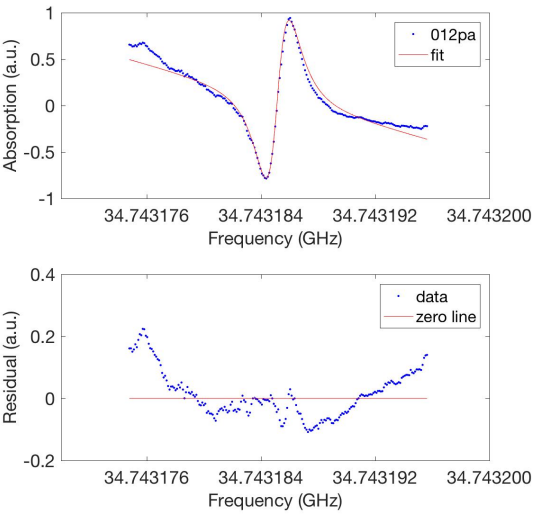

(d)

Figure 3.20: Riga1 absorption dispersion, fitted curve and residual plot for 1pa, 2pa, 4pa e 12pa in the Lamb dip proximity with wavelength modulation technique

Chapter 4

Absolute frequency stabilization of a QCL to saturated absorption of CHF_3

Quantum cascade lasers (QCLs), in particular room-temperature distributed-feedback (DFB) lasers, are becoming the usual sources for accessing mid-IR spectral region for applications ranging from high-sensitivity spectroscopy to frequency metrology, environmental sensing, cold atoms, and molecule control.

For advanced applications in precision spectroscopy, it is need to develop a technique enabling not only the narrowing of the QCL emission down to the kilohertz level but also its referencing to a stable frequency standard. Indeed, although the intrinsic emission linewidth of a QCL can be as low as a few hundred hertz [65] [66], excess technical noise, such as the pump current noise, and internally induced QCL structure noise [67], broadens the QCL emission linewidth by several orders of magnitude up to few megahertz for 1 ms observation times. We present an approach to a narrow emission, absolutely referenced mid-IR QCL. It exploits the availability of a natural ruler of frequency references given by the many strong molecular absorption lines, whose center frequency can be absolutely measured with a sub-kilohertz precision.

4.1 Experimental setup

A Quantum Cascade Laser (QCL) with a tunable frequency from 1155 cm^{-1} to 1160 cm^{-1}, with an optical power up to 40 mW and a linewidth of 1 MHz is used as probe beam. After emerging from a 30-dB optical isolator, the QCL output beam is collimated by a ZnSe plano-convex lens (200mm focal length) followed by a 50/50 beam splitter (BS1) whose reflection propagates as the strong pump beam through a 25 cm long stainless-steel cell (equipped with anti-reflection coated ZnSe windows) containing the CHF_3 gas sample (98% purity) at room temperature, T_{room}, with a measured beam waist diameter of 2.1 mm in the middle of the absorption cell. Reflection from a second 50/50 beam splitter (BS2) is directed to

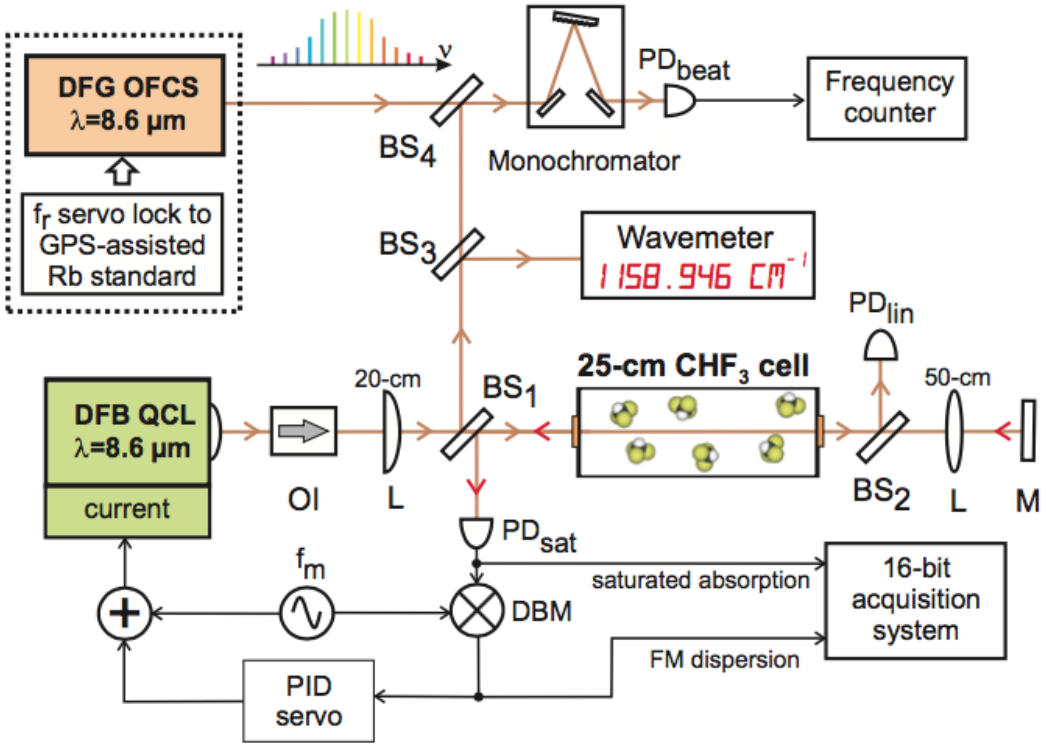

Figure 4.1: Experimental setup

a liquid-nitrogen-cooled HgCdTe (MCT) detector (1 MHz electrical bandwidth), PDlin, to record the single-pass absorption; reflection from BS2 passes through a 50 mm focusing lens and it is back-reflected by a mirror to generate the counter-propagating weak probe beam (1/4 of the pump beam power) which is then superimposed to the pump beam in the gas cell with matched phase fronts (probe beam waist diameter of 1.8 mm). To detect the saturated absorption signal, the probe beam is transmitted by BS1 onto a four-stage thermo-electrically cooled MCT detector (50 MHz bandwidth), PDsat. In order to measure the absolute line-center frequency of a given CHF_3 transition, the QCL frequency is first locked to the zero of the corresponding (dispersive) FM saturated absorption signal using a proportional-integrative-derivative (PID) servo controller acting on the QCL driving current. Then, the frequency-stabilized QCL is beaten against a suitable mid- infrared (MIR) OFCS covering the 8-14 μm spectral region. The first transmission of BS1 is superimposed to the Difference Frequency Generation Optical Frequency Comb (DFG-OFC) at $8.6\mu m$ whose repetition frequency is stabilized against a radio-frequency (RF) synthesizer locked, in turn, to a GPS-disciplined Rb clock; this latter frequency-reference chain has a fractional frequency stability (1-s Allan deviation) and accuracy of $8 \cdot 10^{12}$ and 10^{13}, respectively. After filtering by means of a 0.01 μm monochromator, the combined beams are focused onto a 200 MHz bandwidth MCT detector, PDbeat, ($5.7{\cdot}10^4$ V/W responsivity and 50 nV/pHz noise floor at a temperature of 77 K).

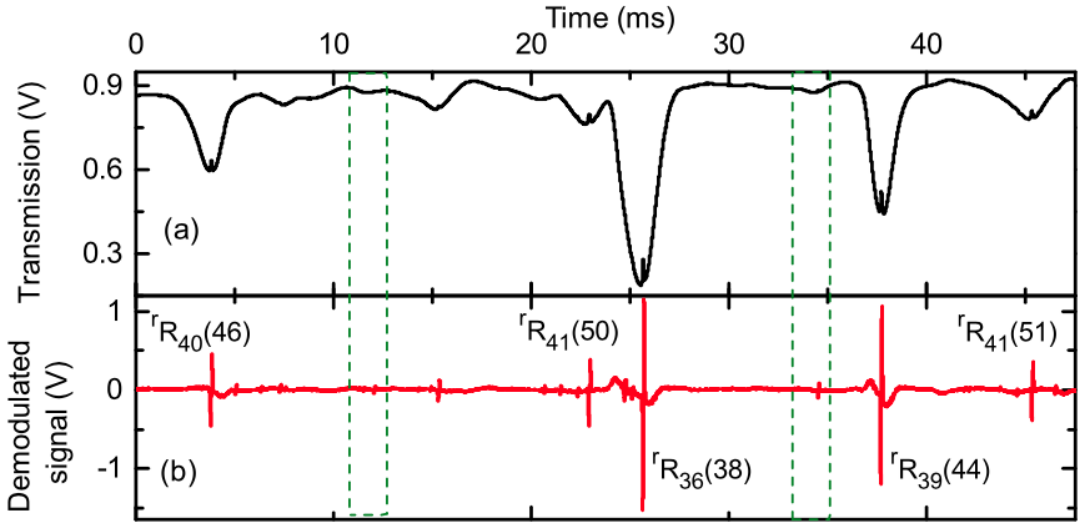

Figure 4.2: Saturated absorption (a)and FM dispersive (b)signal from a 25-cm-long cell filled with CHF_3 gas sample at 10 Pa.

4.2 QCL lock to saturated absorption

In order to perform a frequency modulation spectroscopy method, the input current to the QCL has been modulated at frequency f_m = 1.56 MHz with an amplitude of 0.006 V with a digital Lock-in amplifier. Thanks to the current to frequency conversion of QCL, a modulation in amplitude of input current correspond to a frequency modulation of the probe beam. Thanks to the steep zero crossing and high signal to noise ratio, the first derivative of saturated absorption signal is a good reference for accurate stabilization of the laser frequency of the QCL. Recoded signal from PD_{sat} is sent back to the lock-in amplifier that demodulate signal and, thanks to it is build in PID controller, it can lock to zero the retrieved first derivative signal.

Figure 4.3.a shows the RF spectrum of the photocurrent measured when the QCL is operated in free-running. Three main peaks are clearly distinguished from the background noise: the beat-note signal at f_b ≃53 MHz between the QCL mode and the nearest comb tooth, the comb repetition rate at 250 MHz, and the beat note between the QCL mode and the second nearest comb tooth (at a frequency of ≃197 MHz). The main beat note, observed with a SNR of 40 dB, is characterized by a FWHM linewidth of 600 kHz for an integration time of 50 μs (blue curve in Fig. 3 (b)).

Further linewidth narrowing of the beat note, down to 100 kHz, is obtained when the QCL is frequency stabilized against the FM saturated absorption signal, for example of the ^{r}R38 (36) ro-vibrational component (red curve in Fig. 4.3.b). The 100-kHz QCL line narrowing is mainly limited by the 350-kHz control-loop bandwidth, which turns out to be strictly linked to the FM demodulation electronics finite bandwidth of 100 kHz.

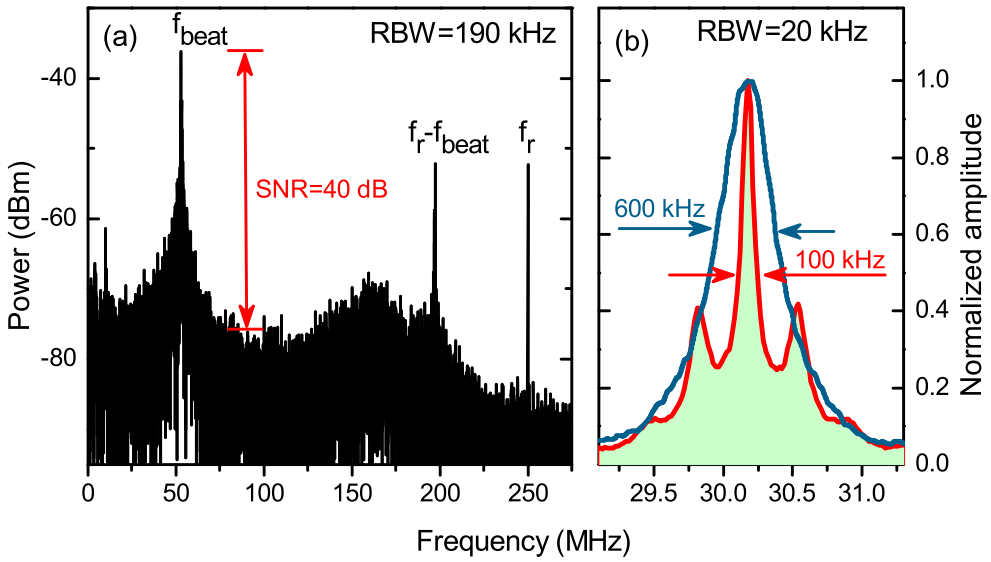

Figure 4.3: RF spectrum of the beat signal between the MIR OFCS and the QCL: (a) QCL in free-running operation (frequency span from DC to 260 MHz, 190 kHz resolution bandwidth); (b) QCL frequency stabilized against the FM saturated absorption of the rR36(38) line: as inferred by the spectral position of the servo bumps, here the closed-loop bandwidth is ∼ 350 kHz.

4.3 Experimental result

To characterize the frequency stability of the Lamb-dip- locked QCL, the main beat note frequency was directly measured by a reciprocal electronic counter without any additional phase-locked-loop (transfer oscillator method). Figure 4.4.a shows the corresponding Allan deviation (open circles) versus the integration time, t, when the QCL is locked against the ^{r}R36(38) line for a CHF_3 pressure of 7 Pa (corresponding to the maximum SNR). In the same diagram, the Allan deviation of the Rb clock (black curve), measured against a hydrogen maser, is also reported for comparison. The QCL Allan deviation reaches a minimum value of $8.6 \cdot 10^{12}$ at t= 1 s,which turns out to be limited by the frequency stability of the adopted Rb clock. For shorter integration times, the stability is characterized by a white phase noise contribution, $\sigma(\tau) = 10^{12} \cdot \tau^{-1}$, indicating a tight phase-locking between the QCL and the Lamb-dip reference. For t > 1 s, a linear drift of 4.5 kHz/min limits the long-term stability of the frequency stabilized QCL; this drift, essentially due to the air-pressure-induced shift caused by the relatively high leakage (0.14 Pa/min) from the gas cell, prevented us from extending the duration of these measurement sets far above 100 s. By removing from the data the measured linear frequency drift, the Allan deviation is limited at the level of $8 \cdot 10^{12}$ by a flicker frequency noise contribution.

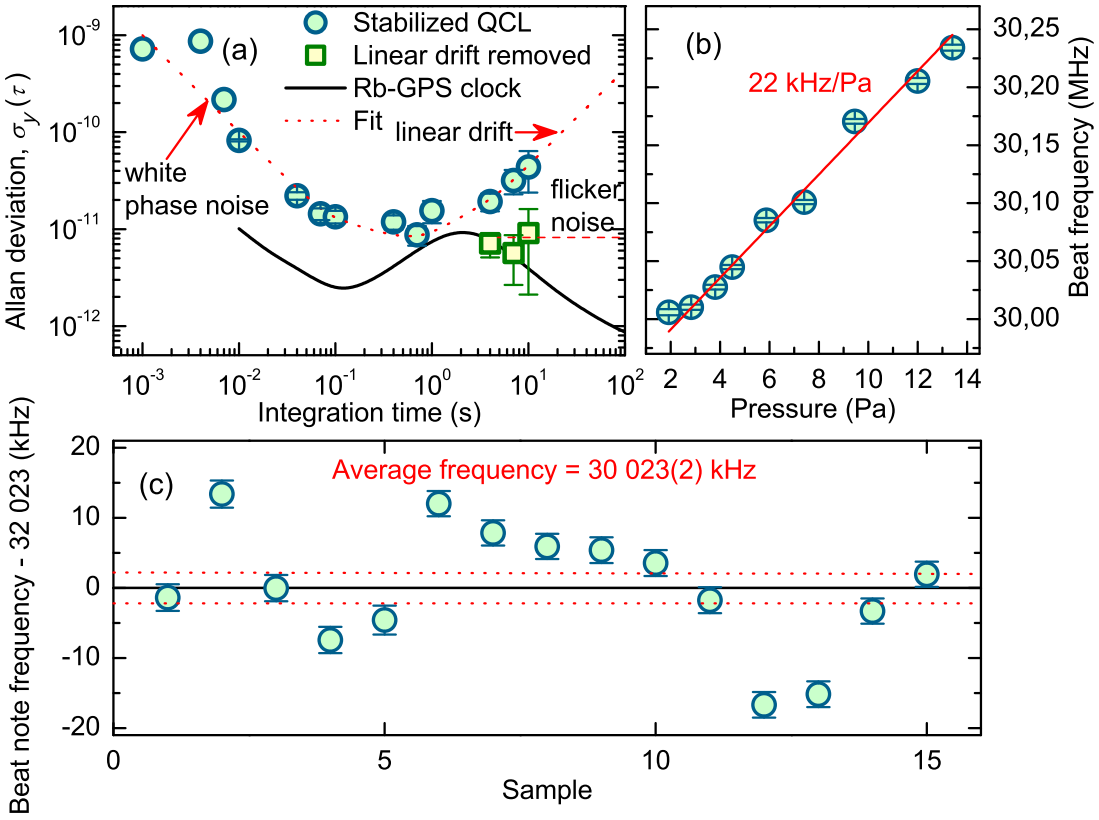

Figure 4.4: Absolute frequency measurements.(a)Allan deviation of the Lamb-dip-locked QCL frequency versus the integration time. The dotted red line represents the best interpolation curve, $\sigma_y^2(\tau) = 10^{-24}/\tau^2 + 0.6 \cdot 10^{-22} + 6 \cdot 10^{-24}\tau^2$. (b) Pressure shift measurement of the $^rR36(38)$ line. (c) Reproducibility in the line-center frequency determination for different measurement sets, carried out under the same experimental conditions. The error bars represent the combined (type A and B) uncertainty whereas the dotted red line is the rms of the average value.

4.4 Uncertainty budget

Afterwards, to thoroughly investigate any systematic effects in the line center frequency determinations, we also measured the sensitivity coefficient of the Lamb-dip-locked QCL frequency against the CHF_3 pressure and gas cell leakage, the pump and probe beam powers, the modulation frequency and depth, the electronic offsets, and the etalon effects.

The other sensitivity coefficients, together with their influence on the systematic (type B) uncertainty of the absolute line-center frequency measurement, are listed in Table 1. Such an analysis reveals that the major sources of type B uncertainties are due to the 0.5% accuracy of the absolute pressure gauge used in the experiments and the measured pressure shift coefficient (corresponding to 0.75 kHz), and to the gas cell leak- age during the measurement time (1.5 kHz). Taking into account all the contributions, the estimated total type B uncertainty is 1.8 kHz, corresponding to a fractional accuracy of $5{\cdot}10^{-11}$.

Finally, to check the reproducibility of the line-center frequency determination, for fixed experimental operating parameters (p_{CHF_3}= 7.00 ± 0.04 Pa, T_{room}= 22.1±0.5℃, P_{pump}= 5mW,P_{probe}= 1.3 mW,f_m= 1.56 MHz, a_m= 1.5 MHz), repeated measurements were performed with an integration time of 1 s (corresponding to the minimum Allan deviation) and a measurement time of 100 s. Figure 4.4 reports fifteen independent measurements as performed over a few days, returning a rms deviation of 2.3 kHz ($6.6{\cdot}10^{11}$), in a good agreement with the estimated type B uncertainty. The measured average frequency of the QCL stabilized is 34 743 125 035(2) kHz (n = 138 972 and fr = 250 001 115.75 Hz). Taking into account the pressure-shift coefficient, the line-center frequency of the ^{r}R36 (38) transition extrapolated at zero pressure is 34 743 124 881(2) kHz (1 158.905 901 53(8) cm^{-1}). [68]

Parameter	Coefficient	Type B uncertanty
CHF_3 preassure, p_{CHF_3}	22(1) kHz/Pa	0.75 kHz
gas cell leakege, p_{leak}	38(2) kHz/Pa	1.5 kHz
laser power, P_{QCL}	45 kHz/mW	0.2 kHz
modulation frequency, f_m	100 Hz/kHz	negligible
modulation depth, a_m	16 kHz/MHz	negligible
electronic offset	0.3 kHz/mV	0.2 kHz
etalon/interference effects		0.5 kHz
Rb-GPS-clock		0.04 kHz
Total type B uncertainty		1.8 kHz ($5{\cdot}10^{11}$)

Table 4.1: Measured sensitivity coefficients for the ^{r}R36(38) line and their contribution to the uncertainty budget.
[68]

Conclusion and perspectives

This experimental thesis reports absolute frequency measurements of the sub-Doppler absorption lines of CHF_3 using a quantum cascade laser and an optical frequency comb in two different methodologies. The first, providing the absolute frequency stabilization of the QCL to saturated absorption line, demonstrate a fractional precision and accuracy of $8{\cdot}10^{-12}$ and $5{\cdot}10^{-11}$ respectively, mainly limited by the stability and by the reproducibility of the developed frequency-modulation non-linear spectrometer. This method can be immediately extended to realize a compact and fully transportable molecular-gas-cell optical frequency standard in the mid-infrared with a potential accuracy at the 10^{-12} level.
The second technique, based on the frequency stabilization of the QCL against the optical frequency comb, demonstrates a very high resolution both in frequency and intensity of the recorded spectral profiles. Due to the high fidelity of the recorded sub-Doppler line-shapes a more sophisticated line profiles have to be employed to better interpolate these experimental data. However, using a single Lorentzian profile for the sub-Doppler features, pressure broadening effects have benn preliminary obtained.
The final aim of these spectroscopic measurements is the determination of the β-ratio between electron and proton masses. To further increase the frequency-resolution and accuracy in the determination of the line-center frequencies an improved version of the experiment is under development based on cold CHF_3 molecules. In particular, by using a 77 K hermetic gas cell, it will be possible to record low-rotational number CHF_3 transitions at pressure lower than 1 Pa characterized by linewidth narrower than 100 kHz. In addiction, combining the cold cell with an optical cavity also two-photon spectroscopy will be performed to increase the signal to noise ratio with respect to conventional pump-probe non-linear spectroscopy setup.

Peer reviewed publications

- *Absolute frequency measurements of CHF_3 Doppler-free ro-vibrational transitions at 8.6 μm* - Gambetta A, Vicentini E, Wang Y, Coluccelli N, Fasci E, Gianfrani L, Castrillo A, Di Sarno V, Santamaria L, Maddaloni P, De Natale P, Laporta P, Galzerano G. Optics Letters, 42(10), 1911-1914.
- *Metrology grade sub.Doppler spectroscopy of CHF_3 a 8.6 μm.* Gambetta A, Vicentini E, Wang, Y., Coluccelli N, Fernandez TT, Fasci E., Castillo A, Gianfrani L, Santamaria L, Di Sarno V, Maddaloni P, Laporta P and Galzerano G. (OSA conference proceeding, CLEO Europe 2017).

Bibliography

[1] John L Hall. Nobel lecture: Defining and measuring optical frequencies. *Reviews of Modern Physics*, 78(4):1279, 2006.

[2] Theodor W Hänsch. Nobel lecture: passion for precision. *Reviews of Modern Physics*, 78(4):1297, 2006.

[3] Scott A Diddams. The evolving optical frequency comb. *JOSA B*, 27(11): B51–B62, 2010.

[4] Chad Orzel. Searching for new physics through atomic, molecular and optical precision measurements. *Physica Scripta*, 86(6):068101, 2012.

[5] Savely Karshenboim and Ekkehard Peik. An introduction to varying fundamental constants. *Astrophysics, Clocks and Fundamental Constants*, pages 1–18, 2004.

[6] William Marciano. Time varying fundamental constants, extra dimensionsand the renormalization group. *Astrophysics, Clocks and Fundamental Constants*, pages 97–105, 2004.

[7] Jean-Philippe Uzan. The fundamental constants and their variation: observational and theoretical status. *Reviews of modern physics*, 75(2):403, 2003.

[8] E Peik, B Lipphardt, H Schnatz, Chr Tamm, S Weyers, and R Wynands. Laboratory limits on temporal variations of fundamental constants: an update. *arXiv preprint physics/0611088*, 2006.

[9] W Ubachs, R Buning, KSE Eikema, and E Reinhold. On a possible variation of the proton-to-electron mass ratio: H 2 spectra in the line of sight of high-redshift quasars and in the laboratory. *Journal of molecular spectroscopy*, 241(2):155–179, 2007.

[10] E Reinhold, R Buning, U Hollenstein, A Ivanchik, P Petitjean, and W Ubachs. Indication of a cosmological variation of the proton-electron mass ratio based on laboratory measurement and reanalysis of h 2 spectra. *Physical Review Letters*, 96(15):151101, 2006.

[11] L Santamaria, V Di Sarno, I Ricciardi, S Mosca, M De Rosa, Gabriele Santambrogio, P Maddaloni, and P De Natale. Assessing the time constancy

of the proton-to-electron mass ratio by precision ro-vibrational spectroscopy of a cold molecular beam. *Journal of Molecular Spectroscopy*, 300:116–123, 2014.

[12] Piers Forster, Venkatachalam Ramaswamy, Paulo Artaxo, Terje Berntsen, Richard Betts, David W Fahey, James Haywood, Judith Lean, David C Lowe, Gunnar Myhre, et al. Changes in atmospheric constituents and in radiative forcing. chapter 2. In *Climate Change 2007. The Physical Science Basis*. 2007.

[13] O. Svelto. *Principles of Lasers*. Springer US, 2012. ISBN 9781461576679.

[14] M. Nisoli and S.E. Esculapio. *Semiconductor Photonics: Principles and Applications*. Società Editrice Esculapio, 2016. ISBN 9788893850025.

[15] Wolfgang Demtröder. *Laser spectroscopy: basic concepts and instrumentation*. Springer Science & Business Media, 2013.

[16] Norman F Ramsey. A molecular beam resonance method with separated oscillating fields. *Physical Review*, 78(6):695, 1950.

[17] G Graner and G Guelachvili. Fluoroform: The polyad at 8–9 μm. *Journal of Molecular Spectroscopy*, 107(2):215–228, 1984.

[18] T.J. Quinn, T.J. Quinn, S. Leschiutta, P. Tavella, and Società italiana di fisica. *Recent Advances in Metrology and Fundamental Constants: Varenna on Lake Como, Villa Monastero, 25 July-4 August 2000*. Proceedings of the International School of Physics "Enrico Fermi". IOS Press, 2001. ISBN 9781586031671. URL `https://books.google.it/books?id=WE22Fez60EcC`.

[19] LO Hocker, A Javan, D Ramachandra Rao, L Frenkel, and T Sullivan. Absolute frequency measurement and spectroscopy of gas laser transitions in the far infrared. *Applied Physics Letters*, 10(5):147–149, 1967.

[20] H Schnatz, B Lipphardt, J Helmcke, F Riehle, and G Zinner. First phase-coherent frequency measurement of visible radiation. *Physical Review Letters*, 76(1):18, 1996.

[21] JN Eckstein, AI Ferguson, and TW Hänsch. High-resolution two-photon spectroscopy with picosecond light pulses. *Physical Review Letters*, 40(13): 847, 1978.

[22] Jun Ye. *Femtosecond optical frequency comb: principle, operation and applications*. Springer Science & Business Media, 2005.

[23] Scott A Diddams, David J Jones, Jun Ye, Steven T Cundiff, John L Hall, Jinendra K Ranka, Robert S Windeler, Ronald Holzwarth, Thomas Udem, and TW Hänsch. Direct link between microwave and optical frequencies with a 300 thz femtosecond laser comb. *Physical Review Letters*, 84(22):5102, 2000.

[24] SA Meyer, JA Squier, and Scott A Diddams. Diode-pumped yb: Kyw femtosecond laser frequency comb with stabilized carrier-envelope offset frequency. *The European Physical Journal D-Atomic, Molecular, Optical and Plasma Physics*, 48(1):19–26, 2008.

[25] MC Stumpf, S Pekarek, A EH Oehler, T Südmeyer, JM Dudley, and U Keller. Self-referencable frequency comb from a 170-fs, 1.5-μm solid-state laser oscillator. *Applied Physics B: Lasers and Optics*, 99(3):401–408, 2010.

[26] Sergey B Mirov, VV Fedorov, DV Martyshkin, IS Moskalev, MS Mirov, and VP Gapontsev. Progress in mid-ir cr 2+ and fe 2+ doped ii-vi materials and lasers. *Optical Materials Express*, 1(5):898–910, 2011.

[27] Nikolai Tolstik, Evgeni Sorokin, and Irina T Sorokina. Kerr-lens mode-locked cr: Zns laser. *Optics letters*, 38(3):299–301, 2013.

[28] Evgueni Slobodtchikov and Peter Moulton. Progress in ultrafast cr: Znse lasers. In *Advanced Solid-State Photonics*, pages AW5A–4. Optical Society of America, 2012.

[29] Davide Gatti, Tommaso Sala, Marco Marangoni, Gianluca Galzerano, and Livio Gianfrani. Precision molecular spectroscopy with frequency combs. *Encyclopedia of Analytical Chemistry*, 2012.

[30] Florian Tauser, Alfred Leitenstorfer, and Wolfgang Zinth. Amplified femtosecond pulses from an er: fiber system: Nonlinear pulse shortening and self-referencing detection of the carrier-envelope phase evolution. *Optics express*, 11(6):594–600, 2003.

[31] Brian R Washburn, Scott A Diddams, Nathan R Newbury, Jeffrey W Nicholson, Man F Yan, and Carsten G Jørgensen. Phase-locked, erbium-fiber-laser-based frequency comb in the near infrared. *Optics letters*, 29(3):250–252, 2004.

[32] H Lim, J Buckley, A Chong, and FW Wise. Fibre-based source of femtosecond pulses tunable from 1.0 to 1.3 μm. *Electronics Letters*, 40(24):1523–1525, 2004.

[33] Parama Pal, Wayne H Knox, Ingmar Hartl, and Martin E Fermann. Self referenced yb-fiber-laser frequency comb using a dispersion micromanaged tapered holey fiber. *Optics express*, 15(19):12161–12166, 2007.

[34] I Hartl, LB Fu, BK Thomas, L Dong, ME Fermann, J Kim, FX Kartner, and C Menyuk. Self-referenced f ceo stabilization of a low noise femtosecond fiber oscillator. In *Lasers and Electro-Optics, 2008 and 2008 Conference on Quantum Electronics and Laser Science. CLEO/QELS 2008. Conference on*, pages 1–2. IEEE, 2008.

[35] JHV Price, K Furusawa, TM Monro, L Lefort, and DJ Richardson. Tunable, femtosecond pulse source operating in the range 1.06–1.33 μm based on an yb 3+-doped holey fiber amplifier. *JOSA B*, 19(6):1286–1294, 2002.

[36] LE Nelson, EP Ippen, and HA Haus. Broadly tunable sub-500 fs pulses from an additive-pulse mode-locked thulium-doped fiber ring laser. *Applied physics letters*, 67(1):19–21, 1995.

[37] Max A Solodyankin, Elena D Obraztsova, Anatoly S Lobach, Alexander I Chernov, Anton V Tausenev, Vitaly I Konov, and Evgueni M Dianov. Mode-locked 1.93 μm thulium fiber laser with a carbon nanotube absorber. *Optics letters*, 33(12):1336–1338, 2008.

[38] K Kieu and FW Wise. Soliton thulium-doped fiber laser with carbon nanotube saturable absorber. *IEEE Photonics Technology Letters*, 21(3):128–130, 2009.

[39] Frithjof Haxsen, Dieter Wandt, Uwe Morgner, Joerg Neumann, and Dietmar Kracht. Pulse characteristics of a passively mode-locked thulium fiber laser with positive and negative cavity dispersion. *Optics express*, 18(18):18981–18988, 2010.

[40] Qing Wang, Jihong Geng, Zhuo Jiang, Tao Luo, and Shibin Jiang. Mode-locked tm-ho-codoped fiber laser at 2.06 μm. *IEEE Photonics Technology Letters*, 23(11):682–684, 2011.

[41] Daniel Hofstetter and Jérôme Faist. High performance quantum cascade lasers and their applications. *Solid-State Mid-Infrared Laser Sources*, pages 61–98, 2003.

[42] Roberto Paiella, Federico Capasso, Claire Gmachl, Deborah L Sivco, James N Baillargeon, Albert L Hutchinson, Alfred Y Cho, and HC Liu. Self-mode-locking of quantum cascade lasers with giant ultrafast optical nonlinearities. *Science*, 290(5497):1739–1742, 2000.

[43] Christine Y Wang, Lyuba Kuznetsova, VM Gkortsas, Laurent Diehl, Franz X Kaertner, Mikhail A Belkin, Alexey Belyanin, Xiaofeng Li, Donhee Ham, Harald Schneider, et al. Mode-locked pulses from mid-infrared quantum cascade lasers. *Optics Express*, 17(15):12929–12943, 2009.

[44] Albert Schliesser, Nathalie Picqué, and Theodor W Hänsch. Mid-infrared frequency combs. *Nature Photonics*, 6(7):440–449, 2012.

[45] Cornelia Fischer and Markus Sigrist. Mid-ir difference frequency generation. *Solid-state mid-infrared laser sources*, pages 99–143, 2003.

[46] P Maddaloni, P Malara, G Gagliardi, and P De Natale. Mid-infrared fibre-based optical comb. *New Journal of Physics*, 8(11):262, 2006.

[47] Seth M Foreman, David J Jones, and Jun Ye. Flexible and rapidly configurable femtosecond pulse generation in the mid-ir. *Optics letters*, 28(5): 370–372, 2003.

[48] Christian Erny, K Moutzouris, Jens Biegert, Dietrich Kühlke, Florian Adler, A Leitenstorfer, and U Keller. Mid-infrared difference-frequency generation of ultrashort pulses tunable between 3.2 and 4.8 μm from a compact fiber source. *Optics letters*, 32(9):1138–1140, 2007.

[49] Alessio Gambetta, Roberta Ramponi, and Marco Marangoni. Mid-infrared optical combs from a compact amplified er-doped fiber oscillator. *Optics letters*, 33(22):2671–2673, 2008.

[50] Axel Ruehl, Alessio Gambetta, Ingmar Hartl, Martin E Fermann, Kjeld SE Eikema, and Marco Marangoni. Widely-tunable mid-infrared frequency comb source based on difference frequency generation. *Optics letters*, 37(12):2232–2234, 2012.

[51] KL Vodopyanov, E Sorokin, IT Sorokina, and PG Schunemann. Mid-ir frequency comb source spanning 4.4–5.4 μm based on subharmonic gaas optical parametric oscillator. *Optics letters*, 36(12):2275–2277, 2011.

[52] Samuel T Wong, Konstantin L Vodopyanov, and Robert L Byer. Self-phase-locked divide-by-2 optical parametric oscillator as a broadband frequency comb source. *JOSA B*, 27(5):876–882, 2010.

[53] Nick Leindecker, Alireza Marandi, Robert L Byer, Konstantin L Vodopyanov, Jie Jiang, Ingmar Hartl, Martin Fermann, and Peter G Schunemann. Octave-spanning ultrafast opo with 2.6-6.1 μm instantaneous bandwidth pumped by femtosecond tm-fiber laser. *Optics express*, 20(7):7046–7053, 2012.

[54] Anatoliy A Savchenkov, Andrey B Matsko, Dmitry Strekalov, Makan Mohageg, Vladimir S Ilchenko, and Lute Maleki. Low threshold optical oscillations in a whispering gallery mode c a f 2 resonator. *Physical review letters*, 93(24):243905, 2004.

[55] TJ Kippenberg, SM Spillane, and KJ Vahala. Kerr-nonlinearity optical parametric oscillation in an ultrahigh-q toroid microcavity. *Physical review letters*, 93(8):083904, 2004.

[56] P DelHaye, A Schliesser, O Arcizet, T Wilken, R Holzwarth, and TJ Kippenberg. Optical frequency comb generation from a monolithic microresonator. *Nature*, 450(7173):1214–1217, 2007.

[57] Pascal DelHaye, T Herr, E Gavartin, ML Gorodetsky, Ronald Holzwarth, and Tobias J Kippenberg. Octave spanning tunable frequency comb from a microresonator. *Physical Review Letters*, 107(6):063901, 2011.

[58] G Méjean, S Kassi, and D Romanini. Measurement of reactive atmospheric species by ultraviolet cavity-enhanced spectroscopy with a mode-locked femtosecond laser. *Optics letters*, 33(11):1231–1233, 2008.

[59] Elisabeth Peters, Scott A Diddams, Peter Fendel, Sascha Reinhardt, TW Hänsch, and Th Udem. A deep-uv optical frequency comb at 205 nm. *Optics express*, 17(11):9183–9190, 2009.

[60] Arman Cingöz, Dylan C Yost, Thomas K Allison, Axel Ruehl, Martin E Fermann, Ingmar Hartl, and Jun Ye. Direct frequency comb spectroscopy in the extreme ultraviolet. *Nature*, 482(7383):68–71, 2012.

[61] Jerome Faist, Federico Capasso, Deborah L Sivco, Carlo Sirtori, Albert L Hutchinson, Alfred Y Cho, et al. Quantum cascade laser. *Science*, 264 (5158):553–556, 1994.

[62] James P Gordon. Theory of the soliton self-frequency shift. *Optics letters*, 11(10):662–664, 1986.

[63] Ben-Jan Hong and Chih-Chung Yang. Interactions between femtosecond solitons in optical fibers. *JOSA B*, 8(5):1114–1121, 1991.

[64] Alessio Gambetta, Nicola Coluccelli, Marco Cassinerio, Davide Gatti, Paolo Laporta, Gianluca Galzerano, and Marco Marangoni. Milliwatt-level frequency combs in the 8–14 μm range via difference frequency generation from an er: fiber oscillator. *Optics letters*, 38(7):1155–1157, 2013.

[65] S Bartalini, S Borri, I Galli, G Giusfredi, D Mazzotti, T Edamura, N Akikusa, M Yamanishi, and P De Natale. Measuring frequency noise and intrinsic linewidth of a room-temperature dfb quantum cascade laser. *Optics express*, 19(19):17996–18003, 2011.

[66] Lionel Tombez, J Di Francesco, Stéphane Schilt, Gianni Di Domenico, Jérôme Faist, P Thomann, and D Hofstetter. Frequency noise of free-running 4.6 μm distributed feedback quantum cascade lasers near room temperature. *Optics letters*, 36(16):3109–3111, 2011.

[67] Lionel Tombez, Stéphane Schilt, Joab Di Francesco, Pierre Thomann, and Daniel Hofstetter. Temperature dependence of the frequency noise in a mid-ir dfb quantum cascade laser from cryogenic to room temperature. *Optics express*, 20(7):6851–6859, 2012.

[68] Alessio Gambetta, Edoardo Vicentini, Yuchen Wang, Nicola Coluccelli, Eugenio Fasci, Livio Gianfrani, Antonio Castrillo, Valentina Di Sarno, Luigi Santamaria, Pasquale Maddaloni, et al. Absolute frequency measurements of chf 3 doppler-free ro-vibrational transitions at 8.6 μm. *Optics Letters*, 42 (10):1911–1914, 2017.